

# Large deformation electrohydrodynamics of a Skalak elastic capsule in AC electric field

Sudip Das, Rochish M Thaokar\*

*Department of Chemical Engineering, Indian Institute of Technology Bombay, Mumbai 400 076, India*

(Dated: February 4, 2022)

The axisymmetric electrohydrodynamic deformation of an elastic capsule with capacitive membrane obeying Skalak law under uniform AC electric field is investigated using analytical and boundary integral theory. The low capillary number (the ratio of destabilizing shear or electric force to the stabilizing elastic force) regime shows time-averaged prolate and oblate spheroid deformations, and the time-periodic prolate-sphere, oblate-sphere breathing modes are commensurate with the time averaged-deformation. A novel prolate-oblate breathing mode is observed due to an interplay of finite membrane charging time and the field reversal of the AC field. The study, when extended to high capillary number, shows new breathing modes of cylinder-prolate, cylinder-oblate, and biconcave-prolate deformation. These are the results of highly compressive normal Maxwell stress at the poles and are aided by weak compressive equatorial stress, characteristic of a capacitive membrane. The findings of this work should form the basis for the understanding of more complex biological cells and synthetic capsules for industrial applications.

## I. Introduction

Elastic capsules and vesicles consist of a thin membrane separating the inner and outer fluids and have been commonly used as bio-mimetic systems to understand the mechanics of biological cells [19, 20], which are much more complex. Elastic capsules form good models for cells such as red blood cells. Moreover, they are used in technological applications such as microreactors [60] and diagnostics applications [57, 59]. Therefore, exploring the mechanical and rheological behavior of an elastic capsule is an important topic of research [6, 31, 50].

Vesicles consist of a lipid bilayer membrane which resists deformation by bending stress [32, 61]. The lipid bilayers are characterized by negligible shear elasticity but are area conserving [21, 46], which leads to the generation of a non-uniform but isotropic tension in the membrane corresponding to the imposed stresses. The membrane in elastic capsules, on the other hand, is made up of a crosslinked network of proteins (as in red blood cells) or other surface active molecules. Elastic capsules have a finite shear elasticity and they resist deformation by in-plane shear and dilatational stresses, these are related to the in-plane shear and dilatational strains [5]. The elasticity (shear and dilatation) can generate non-uniform, anisotropic tensions in the membrane. There are other differences between a capsule and a vesicle, for example, while an area preserving spherical vesicle cannot deform, a spherical elastic capsule with a compressible membrane can admit deformations.

The electrohydrodynamics of vesicles have been fairly well investigated in the last few decades in the context of cell electroporation [9, 52], electrofusion as well as cell dielectrophoresis [37, 39, 44] and electrodeformation [26, 27, 34–36, 54]. The electric field models too, for a vesicle, have evolved over the years. While Helfrich modeled the electrostatics of a vesicle subjected

to an electric field by assuming a dielectric drop suspended in a conducting fluid [21, 28], there have been attempts to model it as a leaky dielectric drop in a leaky dielectric fluid [58]. Recently a more realistic capacitor model for electrostatics [12, 27, 47, 48, 54] have been introduced. The capacitor model for electrostatics assumes the vesicle to be made up of an infinitesimally thin dielectric layer characterized by a membrane capacitance and conductance enclosing a leaky dielectric fluid and embedded in another leaky dielectric fluid. Several timescales can then be identified apart from the hydrodynamic timescale. These associated timescales are the charge relaxation timescale of the outer fluid, the time required for the two fluids to behave like leaky dielectrics, namely the Maxwell-Wagner relaxation time and the membrane charging time [34].

AC fields are typically preferred in operations such as electro-deformation and dielectrophoresis involving vesicles and cells. An advantage of AC fields, apart from preventing electrolysis of the solution, is the control of trans-membrane potential in such cells and vesicles [17], thereby preventing electroporation [33] and enabling systematic investigations. Experiments and analytical theories on electrohydrodynamics of vesicles in the low electric field limit show that the variation of deformation with frequency sensitively depends upon the conductivity ratio of the internal and external fluid media [38, 56]. This dependence is due to an interplay of the different electric timescales and the applied frequency. For more conducting inner medium, prolate spheroids and spherical steady shapes are observed, while in the case of more conducting outer medium, spherical, oblate and prolate spheroidal shapes are observed. At high electric fields, experimental investigations [14, 43] showed squaring of a vesicle in a DC field which was reaffirmed and explained by a few 2-D [34, 35] and 3-D [26, 27, 54] computational analyses. Further studies showed that unlike DC fields, a vesicle subjected to high AC electric field showed deformation modes such as breathing and oscillating [36].

\* rochish@che.iitb.ac.in

Theoretical analyses of capsule [1, 3, 4, 16, 18, 25, 51, 55] in the limit of small deformation, indicate a linear relationship between the extent of deformation and the capillary number. In this limit, other aspects of capsule deformation such as orientation, tank-treading motion, and rheology of dilute suspension have also been reported. Several computational analyses of a capsule in external fluid flow in the large deformation limit present the dependence of the deformation on the different membrane constitutive laws [2, 30] and their break up (of a capsule with strain softening membrane) beyond a critical capillary number [2, 7, 11, 13, 41]

Relatively few studies have been reported on the deformation of elastic capsules under DC [18] and AC [51] electric fields. These studies were restricted to small deformation limit. A strong influence of the applied electric field on the deformation of the capsule was reported in the experimental, theoretical and computational analysis of a conducting capsule enclosing a conducting fluid and suspended in a dielectric fluid medium [24]. Moreover, this analysis suggests the usability of the electrohydrodynamics to determine the linear and nonlinear elastic properties of a capsule. A comprehensive analysis of the deformation of an elastic capsule with a dielectric membrane in DC electric field is reported in our earlier work [10] which shows several complex modes of deformation, such as biconcave and hexagonal shapes. These new modes of deformation are not observed in the deformation of vesicles in DC electric field [26, 27, 36, 54].

In this analysis, we investigate the deformation of an elastic capsule in strong AC electric field, wherein an interaction between the electric stress and restoring elastic forces could lead to results different than those obtained for vesicles. Also, the phase diagrams are constructed for deformation of a spherical elastic capsule in low (using both the boundary integral calculation and analytical theory) and high (using boundary integral method) capillary numbers in AC electric field and attempts are made to understand the underlying physics. The capacitor model is used for modeling the electrostatics [22, 26, 27, 34–36, 54] while the capsule is modeled as a strain hardening Skalak membrane [49]. The deformation of an object in AC field has time-averaged and time-periodic parts, and their dependence on frequency could be significantly different. The physics of both these kinds of deformation are analyzed in this work.

## II. Problem description

A spherical capsule is placed in an applied uniform AC electric field in which the direction of the applied field is parallel to the axis of symmetry, the  $y$ -axis (shown in fig. 1). The AC electric field is defined by  $\vec{E}_{AC}^\infty = \vec{E}_0 \cos(\tilde{\omega}\tilde{t})\mathbf{e}_y$ , where  $\vec{E}_0$ , and  $\tilde{\omega}$  are the intensity and frequency of the applied electric field, respectively and  $\tilde{t}$  is the time.

Both the inner and outer fluid media are Newtonian with the outer fluid viscosity  $\mu$  and inner fluid viscosity  $\lambda\mu$ , where  $\lambda$  is the viscosity ratio. Conductivity and

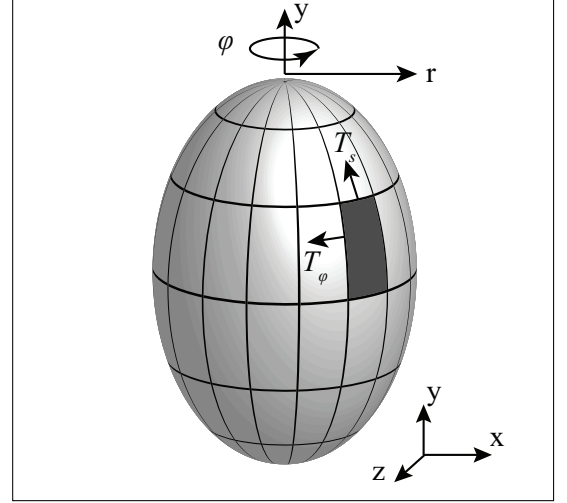


FIG. 1: Schematic representation of an axisymmetrically deformed elastic capsule. The electric field is applied parallel to the  $y$ -axis.  $T_s$  and  $T_\phi$  are meridional and azimuthal membrane tensions, respectively.

dielectric constant of the fluid media are  $\sigma_{i,e}$  and  $\epsilon_{i,e}$ , respectively. In this work, subscripts  $i$  and  $e$  stand for inner and outer fluid media, respectively. Electrical properties used in the computations are described as ratios with respect to the outer fluid media:  $\sigma_r = \sigma_i/\sigma_e$  and  $\epsilon_r = \epsilon_i/\epsilon_e$ . The membrane is considered to be purely elastic with elastic modulus  $E_s$  and it provides resistance to bending deformation proportional to the bending rigidity  $\kappa_b$ . The membrane electrical properties are capacitance  $C_m$  and conductance  $G_m$ .

The charge relaxation time of the external fluid,  $\epsilon_e\epsilon_0/\sigma_e$ , where  $\epsilon_0$  is the permittivity of the free space, is considered as the scaling parameter for time and the velocity of the fluid is scaled by  $E_s/\mu_e$ . Frequency of the applied electric field is scaled by  $\sigma_e/\epsilon_e\epsilon_0$ , the inverse of the parameter used for scaling of time. The intensity of the electric field ( $\tilde{E}$ ), potential ( $\tilde{\phi}$ ), and stress are scaled by  $E_0$ ,  $E_0a$ , and  $E_s/a$ , respectively, where  $a$  is the radius of the capsule. All the variables with and without ( $\sim$ ) represent dimensional and scaled quantities, respectively. In this analysis, the magnitude of the destabilizing force due to the electric field is expressed relative to the stabilizing elastic force by the nondimensional capillary number,  $Ca = a\epsilon_e\epsilon_0E_0^2/E_s$ .

For the simplicity of the calculations, a very thin (assumed to be two dimensional) membrane is considered to be impermeable to both the fluids, thereby keeping the volume of the capsule constant. The effect of the bending rigidity is considered to be important as it prevents the formation of sharp corners as well as helps in computation by averting numerical instabilities [15].

The resultant of the hydrodynamic force and non-hydrodynamic forces due to electric Maxwell stress, elastic force, and force because of resistance to bending cause a change in the shape of a capsule. Stokes equa-

tions are considered as the model equations to study the capsule hydrodynamics [40, 42], electric stresses are calculated by solving Laplace's equation along with normal electric current continuity [26, 27, 34–36]. Membrane elastic forces are determined from the well known Skalak law for the strain hardening membrane [49]. Bending force is a function of up to fourth order derivative of the position of the interface, and it is calculated using the spectral method [29].

### III. Problem formulation

The deformation of a capsule in an AC field is studied analytically using the small deformation theory as well as numerically, using axisymmetric boundary integral method to understand large deformations.

#### A. Boundary integral formulation

The elastic force, electric force, the force due to bending and the hydrodynamic forces are discussed in detail in the following sections.

##### 1. Membrane elasticity

Nonlinear response of a 2D membrane to deformation is modeled by different membrane constitutive laws, namely Generalized Hooke's law, Skalak law, Mooney-Rivlin law, Evan-Skalak law etc., and can be broadly categorized into strain hardening membrane models and strain softening membrane models. In this analysis, the deformation of a capsule is investigated using the Skalak model which exhibits a strain hardening behavior. According to the Skalak law [49], the tension in the principal direction  $i$  (the other principal direction being  $j$ ), can be obtained, in terms of principal extension ratios,  $\lambda_{i,j}$ , as

$$T_i^{SK} = G^{SK} \frac{1}{\lambda_i \lambda_j} [\lambda_i^2 (\lambda_i^2 - 1) + C (\lambda_i \lambda_j)^2 \{(\lambda_i \lambda_j)^2 - 1\}], \quad (1)$$

where  $C$  is the area dilatation parameter for Skalak membrane, larger the value of  $C$ , stiffer is the membrane. In this analysis,  $C = 1$  is considered. The first term, on the right-hand side of eq. (1), is corresponding to the shear deformation with the shear modulus  $G^{SK} = E_s(1 + C)/2(1 + 2C)$  and the second term accounts for the area dilatation with the dilatation modulus  $CG^{SK}$ . Membrane tension in the principal direction  $j$  can be obtained by interchanging indices. In our analysis, principal directions  $i$  and  $j$  correspond to the meridional and azimuthal directions, respectively and the corresponding tensions (force/length) are considered to be  $T_s$  and  $T_\phi$ . These tensions contribute to the normal and

tangential elastic tractions (force/area) as

$$f_n^{el} = -(K_s T_s + K_\phi T_\phi) \quad (2)$$

$$f_t^{el} = \frac{dT_s}{ds} + \frac{1}{r} \frac{dr}{ds} (T_s - T_\phi), \quad (3)$$

such that overall elastic traction acting at the interface is  $\mathbf{f}^{el} = f_n^{el} \mathbf{n} + f_t^{el} \mathbf{t}$ , where  $\mathbf{n}$  and  $\mathbf{t}$  are the outward normal and clockwise tangent vectors, respectively. The arc length in the meridional plane,  $s$ , is measured from the north pole to the south. The principal curvatures are defined as

$$K_s = \left| \frac{d\mathbf{t}}{ds} \right| \quad K_\phi = \frac{n_r}{r}, \quad (4)$$

and the components of the unit tangent and the unit normal in  $r$  and  $y$  directions are calculated as

$$t_r = -n_y = \frac{dr}{ds} \quad t_y = n_r = \frac{dy}{ds}. \quad (5)$$

##### 2. Bending resistance

Although the bending resistance of a capsule with a very thin elastic membrane is small compared to the elastic stresses, it can contribute significantly, especially in regions of high curvature and is also known to prevent numerical elastic instabilities [15] (arising from the large compressive stresses).

The dimensionless traction due to bending is given by

$$\mathbf{f}^b = \hat{\kappa}_b [\Delta_s H + 4H(H^2 - K_G)] \mathbf{n}, \quad (6)$$

where,  $H$  and  $K_G$  are mean curvature and Gaussian curvature, respectively,

$$H = \frac{1}{2}(k_s + k_\phi) \text{ and, } K_G = k_s k_\phi. \quad (7)$$

Nondimensional bending rigidity,  $\hat{\kappa}_b = \kappa_b/a^2 E_s$ , is the bending rigidity modulus relative to the elastic modulus. Laplace Beltrami of the mean curvature in cylindrical coordinate system is defined as

$$\Delta_s H = \nabla_s \cdot (\nabla_s H) = \frac{1}{r |\mathbf{X}_s|} \frac{\partial}{\partial s} \left( \frac{r}{|\mathbf{X}_s|} \frac{\partial H}{\partial s} \right), \quad (8)$$

where  $|\mathbf{X}_s| = \sqrt{\left(\frac{\partial r}{\partial s}\right)^2 + \left(\frac{\partial y}{\partial s}\right)^2}$  [23]. The spectral method is used to calculate higher order derivatives for the calculation of Laplace Beltrami of mean curvature [53].

##### 3. Electrostatics

In an externally applied electric field  $E_0 \cos(\omega t)$ , in the absence of any interacting particle, the potential is given by  $\phi^\infty = -y \cos \omega t$ . The internal and the external potential of the capsule satisfy Laplace equation,  $\nabla^2 \phi_{i,e} = 0$ , where  $\phi_i$  and  $\phi_e$  are internal and external potentials. Using Green's theorem, the solution of the Laplace equation can be obtained in integral forms as [34–36]

$$\frac{1}{2}\phi_i(\mathbf{x}_0) = \int_s [G^E(\mathbf{x}, \mathbf{x}_0) \nabla \phi_i(\mathbf{x}) \cdot \mathbf{n}(\mathbf{x}) - \phi_i(\mathbf{x}) \mathbf{n}(\mathbf{x}) \cdot \nabla G^E(\mathbf{x}, \mathbf{x}_0)] dS(\mathbf{x}), \quad (9)$$

$$\frac{1}{2}\phi_e(\mathbf{x}_0) = \phi^\infty(\mathbf{x}_0) - \int_s [G^E(\mathbf{x}, \mathbf{x}_0) \nabla \phi_e(\mathbf{x}) \cdot \mathbf{n}(\mathbf{x}) - \phi_e(\mathbf{x}) \mathbf{n}(\mathbf{x}) \cdot \nabla G^E(\mathbf{x}, \mathbf{x}_0)] dS(\mathbf{x}), \quad (10)$$

where  $G^E(\mathbf{x}_0, \mathbf{x}) = \frac{1}{4\pi|\hat{\mathbf{x}}|}$  is the Green's function for the Laplace's equation in three-dimensional free space. Here,  $dS(\mathbf{x})$  is the differential surface area,  $\mathbf{x}_0$  and  $\mathbf{x}$  are the source point (singular point) and the load point, respectively and  $\hat{\mathbf{x}} = \mathbf{x} - \mathbf{x}_0$ . Transmembrane potential is defined as the discontinuity of potential across the interface, given by

$$\phi_m = \phi_i - \phi_e. \quad (11)$$

Electrical current continuity across the interface is

$$\sigma_r E_{n,i} + \epsilon_r \frac{dE_{n,i}}{dt} = E_{n,e} + \frac{dE_{n,e}}{dt} = \hat{C}_m \frac{d\phi_m}{dt} + \hat{G}_m \phi_m \quad (12)$$

where  $\hat{C}_m = aC_m/\epsilon_e\epsilon_0$  and  $\hat{G}_m = aG_m/\sigma_e$  are the dimensionless capacitance and conductance of the membrane of the capsule, respectively. Solving eqs. (9) and (10) with the definition of transmembrane potential (eq. (11)) and current continuity (eq. (12)), the transmembrane potential and the internal and external normal and tangential electric fields (defined as  $-\partial\phi/\partial s$ )

can be calculated.

The traction associated with the Maxwell electric stress acting at the interface is  $\tilde{\mathbf{f}}^E = (\tilde{\mathbf{T}}_e^E - \tilde{\mathbf{T}}_i^E) \cdot \mathbf{n} = \tilde{\tau}_n^E \mathbf{n} + \tilde{\tau}_t^E \mathbf{t}$ , where the stress tensor  $\tilde{\mathbf{T}}^E = \epsilon\epsilon_0 \left( \tilde{\mathbf{E}}\tilde{\mathbf{E}} - \frac{1}{2}\tilde{E}^2\mathbf{I} \right)$ ,  $\mathbf{I}$  is the identity tensor. The components of the electric stress in dimensionless form are obtained as

$$\tau_n^E = \frac{1}{2} [(E_{n,e}^2 - E_{t,e}^2) - \epsilon_r (E_{n,i}^2 - E_{t,i}^2)], \quad (13)$$

$$\tau_t^E = E_{n,e}E_{t,e} - \epsilon_r E_{n,i}E_{t,i}, \quad (14)$$

and the components of the electric traction can be obtained as

$$f_y^E = \tau_t^E t_y + \tau_n^E n_y \quad \text{and} \quad f_r^E = \tau_t^E t_r + \tau_n^E n_r. \quad (15)$$

#### 4. Hydrodynamics

The typical size of capsules used in applications is  $\sim 100\mu m$  indicating that hydrodynamics can be described as a low Reynolds number phenomena. Therefore, considering Stokes equations to describe the hydrodynamics, Green's theorem can be used to obtain a boundary integral equation given by

$$\mathbf{u}(\mathbf{x}_0) = -\frac{1}{1+\lambda} \frac{1}{4\pi} \int_s \Delta \mathbf{f}(\mathbf{x}) \cdot \mathbf{G}(\mathbf{x}, \mathbf{x}_0) dS(\mathbf{x}) + \frac{1}{4\pi} \frac{1-\lambda}{1+\lambda} \int_s \mathbf{u}(\mathbf{x}) \cdot \mathbf{Q}(\mathbf{x}, \mathbf{x}_0) \cdot \mathbf{n}(\mathbf{x}) dS(\mathbf{x}), \quad (16)$$

where  $\mathbf{G}(\mathbf{x}, \mathbf{x}_0)$  and  $\mathbf{Q}(\mathbf{x}, \mathbf{x}_0)$  are free space Green's functions for Stokes equations [40, 42].

$$\mathbf{G}(\mathbf{x}, \mathbf{x}_0) = \frac{\mathbf{I}}{|\hat{\mathbf{x}}|} + \frac{\hat{\mathbf{x}}\hat{\mathbf{x}}}{|\hat{\mathbf{x}}|^3}, \quad \mathbf{Q}(\mathbf{x}, \mathbf{x}_0) = -6 \frac{\hat{\mathbf{x}}\hat{\mathbf{x}}\hat{\mathbf{x}}}{|\hat{\mathbf{x}}|^5}, \quad (17)$$

are respectively termed as stokeslet and stresslet. The resultant non-hydrodynamic traction acting at the interface,  $\Delta \mathbf{f} = -(\mathbf{f}^{el} + Ca \mathbf{f}^E + \mathbf{f}^b)$ , is responsible for the deformation of the capsule.

From the known interfacial velocity,  $\mathbf{u}(\mathbf{x})$  at  $t$ , the deformation of the capsule to a new shape at  $t + \Delta t$  can be calculated through the kinematic condition

$$\mathbf{x}(t + \Delta t) = \mathbf{x}(t) + k_f \mathbf{u}(\mathbf{x}) \Delta t, \quad (18)$$

where  $k_f$  is the kinematic factor and  $\Delta t$  is the step size of time used in boundary integral calculations. The kinematic factor depends upon the scaling of the variables.

#### B. Analytical theory

A standard asymptotic expansion in the small parameter, the capillary number, is carried out assuming the deformations to be proportional to the capillary number [51], the details of which are provided in appendix A.

#### IV. Results

TABLE I: Associated time scales and their reciprocals at different conductivity ratios for  $C_m = 50$  and  $\epsilon_r = 1$

$\sigma_r$	$t_{E,i}$	$t_{MW}$	$t_{cap}$	$t_{MW}^{-1}$	$t_{cap}^{-1}$
0.1	10	1.43	525	0.7	0.0019
0.3	3.33	1.30	191.66	0.77	0.0052
0.4	2.5	1.25	150	0.8	0.0067
1	1.0	1.0	75	1.0	0.0133
10	0.1	0.25	30	4.0	0.0333

The typical time scales associated with this prob-

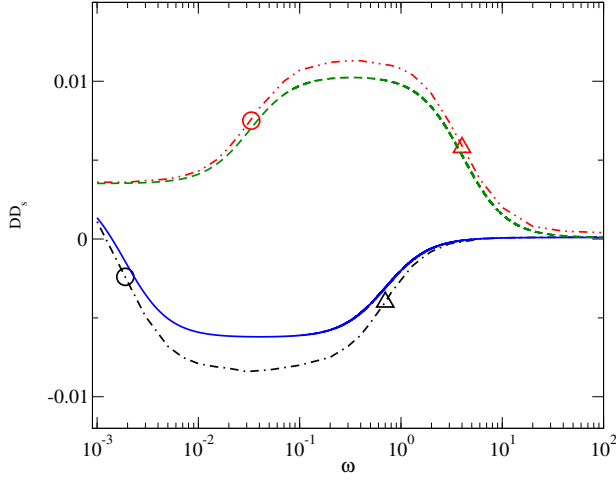


FIG. 2: Time-averaged degree of deformation at  $Ca = 0.01$  as a function of frequency considering  $\epsilon_r = 1$ ,  $G_m = 0$  and  $C_m = 50$ . For  $\sigma_r = 0.1$ , boundary integral and analytical results are shown by  $(-\cdot-)$ , and  $(-)$  curves, respectively and for  $\sigma_r = 10$ , boundary integral and analytical results are shown by  $(\cdot\cdot-)$  and  $(-)$  curves, respectively. Marker points  $\bigcirc$  represent  $t_{cap}^{-1}$  and  $\triangle$  represent  $t_{MW}^{-1}$  for the corresponding curves.

lem are charge relaxation time of the external fluid medium ( $\tilde{t}_E = \epsilon_e \epsilon_0 / \sigma_e$ ), hydrodynamic response time ( $\tilde{t}_H = \mu_e a / E_s$ ), capacitor charging time ( $\tilde{t}_{cap} = a C_m [1/\sigma_i + 1/2\sigma_e]$ ) and the Maxwell-Wagner relaxation time ( $\tilde{t}_{MW} = \epsilon_0 [\epsilon_i + 2\epsilon_e] / [\sigma_i + 2\sigma_e]$ ). We scale time by  $\tilde{t}_E$  and restrict our calculations to the hydrodynamic timescale equal to charge relaxation time of the external fluid medium i.e  $\tilde{t}_H = \tilde{t}_E$ . Therefore, the nondimensional time scales are  $t_E = \tilde{t}_E / \tilde{t}_E = 1$ ,  $t_H = \tilde{t}_H / \tilde{t}_E = 1$ ,  $t_{cap} = \tilde{t}_{cap} / \tilde{t}_E = \hat{C}_m (1/2 + 1/\sigma_r)$  and  $t_{MW} = \tilde{t}_{MW} / \tilde{t}_E = (2 + \epsilon_r) / (2 + \sigma_r)$ . The charge relaxation time of the internal fluid is  $t_{E,i} = t_E (\epsilon_r / \sigma_r)$ . Unless specified, the nondimensional membrane properties are  $\hat{C}_m = 50$ ,  $\hat{G}_m = 0$ , and the ratio of dielectric constants  $\epsilon_r = 1$ . At different conductivity ratios, all the associated time scales are reported in table I. Due to the selection of scaling parameters, the kinematic factor is the inverse of the hydrodynamic timescale, i.e.,  $k_f = 1/t_H$ . In this analysis,  $t_H$  is considered to be unity such that the hydrodynamic response is instantaneous to the changes in electric field.

Figure 3 shows the variation of the maximum transmembrane potential ( $\phi_m$  at the poles) with frequency for the case of  $\sigma_r = 10, 1$ , and  $0.1$ . The expression for the  $\phi_m$  is provided in eq. (A10) which reduces to Schwan equation [45] when  $t_E = \epsilon_e \epsilon_0 / \sigma_e$  and  $t_{E,i} = \epsilon_i \epsilon_0 / \sigma_e \ll t_{cap}$ . From the figure, it can be observed that at very low frequency,  $\phi_m$  is independent of the conductivity ratio and is equal to that of a capsule in DC electric field, which is due to complete charging of a membrane at low frequencies. At very high frequencies, a membrane remains

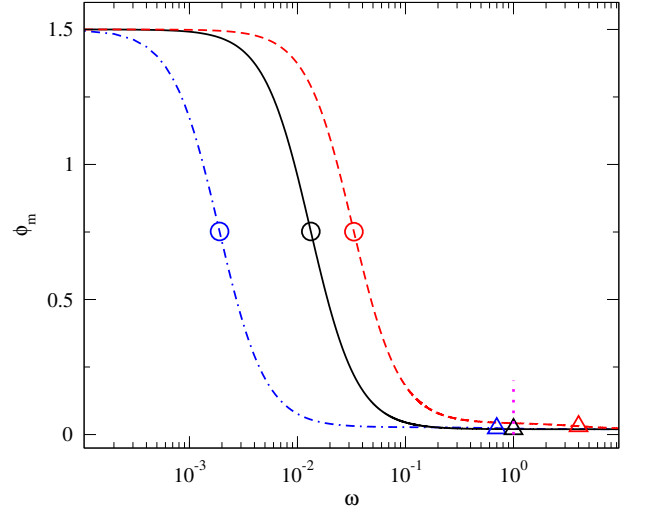


FIG. 3: Maximum value of transmembrane potential as a function of frequency considering  $\epsilon_r = 1$ ,  $G_m = 0$  and  $C_m = 50$  for  $\sigma_r = 0.1$   $(-\cdot-)$ ,  $\sigma_r = 1$   $(-)$  and  $\sigma_r = 10$   $(\cdot\cdot-)$ . Marker points  $\bigcirc$  represent  $t_{cap}^{-1}$  and  $\triangle$  represent  $t_{MW}^{-1}$  for the corresponding curves. Vertical line  $(\cdot\cdot\cdot)$  at  $\omega = 1$  represents  $t_E^{-1}$ .

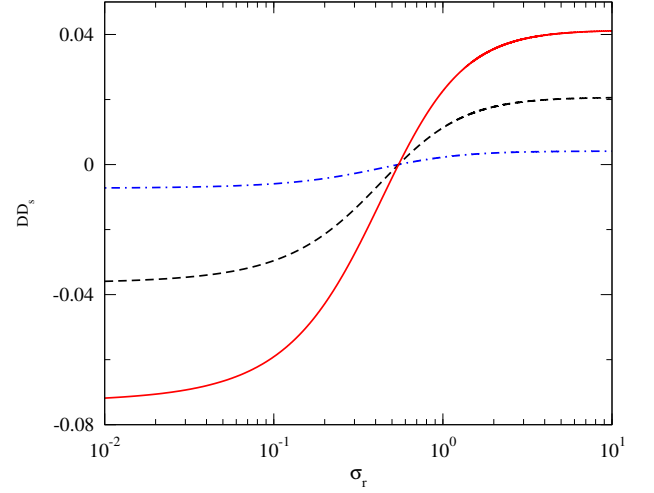


FIG. 4: Time-averaged degree of deformation of a capsule as a function of conductivity ratio at  $Ca = 0.01$   $(-\cdot-)$ ,  $Ca = 0.05$   $(--)$  and  $Ca = 0.1$   $(-)$  considering  $\omega = 0.1$ ,  $\epsilon_r = 1$ ,  $C_m = 50$  and  $G_m = 0$ .

completely uncharged, and thereby  $\phi_m$  attains a small value given by

$$\phi_{m,r} = \frac{3\epsilon_r}{2\hat{C}_m + \epsilon_r(2 + \hat{C}_m)}. \quad (19)$$

The partial charging of a membrane at the intermediate frequencies leads to frequency dependent  $\phi_m$  which increases with  $\sigma_r$ . Therefore, a strong dependence of the deformation on the conductivity ratio is expected.

As a measure of deformation of the capsule, the Tay-

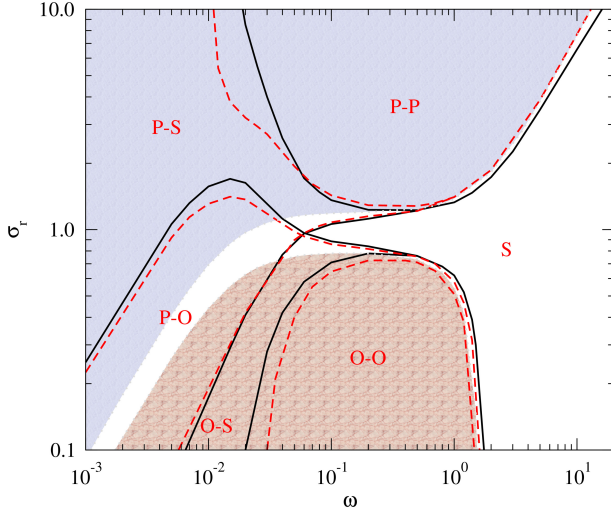


FIG. 5: Phase diagram of time-periodic breathing of a capsule at  $Ca = 0.1$  considering  $\epsilon_r = 1$ ,  $G_m = 0$  and  $C_m = 50$  representing prolate-prolate breathing (P-P), prolate-sphere breathing (P-S), prolate-oblate breathing (P-O), oblate-sphere breathing (O-S), oblate-oblate breathing (O-O), and undeformed sphere (S) zones of the deformation. Continuous curves are numerically obtained boundaries whereas dashed curves are analytically obtained boundaries separating zones of different modes of breathing. Shaded area towards the lower part of the plot represents time-averaged oblate deformation and the shaded area towards the upper part of the plot represents time-averaged prolate deformation.

lor deformation parameter is used, which is defined as the degree of deformation  $DD = \frac{L-B}{L+B}$ , where  $L$  and  $B$  are the diameters of the capsule along the rotational axis of symmetry and at the equator, respectively. The degree of deformation can be decomposed into a stationary (time-averaged) and a time-periodic part  $DD = DD_s + DD_t \cos 2\omega t$ , where the frequency doubling of the deformation is a result of the square dependence of the Maxwell stress on the electric field. The time-averaged degree of deformation as a function of the frequency of the applied electric field, obtained from boundary integral simulation and analytical theory, is compared in fig. 2, for  $\sigma_r = 10$  and  $0.1$  at a low capillary number,  $Ca = 0.01$ .

At very high frequencies,  $\omega \gg t_E^{-1}, t_{MW}^{-1}, t_{cap}^{-1}$ , the electrical impedance of the membrane is negligible, both the fluids behave as dielectrics, and the transmembrane potential is negligible. Therefore, the deformation is almost negligible on account of no dielectric contrast between the inner and the outer fluids, and a spherical geometry is observed.

At frequencies  $\omega > t_{cap}^{-1}$ , the impedance of the membrane is still very low, and the charging of the membrane is governed by the electrical properties of the inner and outer fluid media. The fluids show a leaky dielectric

behavior in the bulk, such that the outer fluid exhibits conductive behavior at frequencies lower than  $t_E^{-1} = 1$ , whereas the inner at frequencies lower than  $t_{E,i}^{-1}$ . As the frequency is lowered, the impedance of the membrane increases and a net interfacial charge build-up starts at a frequency  $t_{MW}^{-1}$ . The interface at frequency  $t_{MW}^{-1}$  is similar to that of a liquid drop on the timescale of  $t_{MW}$  and admits a net free charge and tangential stress. Depending upon the conductivity ratio, the tangential stress can be from poles to the equator ( $\sigma_r < 1$ ) or equator to poles ( $\sigma_r > 1$ ), thereby imparting an oblate spheroid or a prolate spheroid shapes, respectively (fig. 2). This regime also corresponds to the maximum deformation of the capsule.

As the frequency is further decreased,  $\omega < t_{cap}^{-1}$ , the membrane now becomes charged, the membrane impedance is fairly high such that the normal electric fields inside and outside the capsule tend to disappear, on account of the insulating membrane. The tangential stresses, therefore, become negligible and the capsule behaves like a dielectric drop in a conducting fluid. This drop in DC field-like behavior implies that the conductivity ratio does not play a role anymore and prolate spheroids are obtained. A fairly good agreement is obtained between analytical theory (valid at small capillary numbers) and boundary integral calculations.

To verify whether the boundary of the time-averaged prolate to oblate deformation transition is affected by the capillary number,  $DD_s$  vs.  $\sigma_r$  plot is shown for different capillary numbers at a given frequency (fig. 4). For a particular frequency (in this case  $\omega = 0.1$ ), the time-averaged deformation changes from oblate to prolate with an increase in the conductivity ratio. According to the eq. A18, the time-averaged degree of deformation (obtained from analytical theory at small deformation) is proportional to the capillary number and the numerator is only a function of  $\sigma_r$  for the specified  $\epsilon_r, \omega, \hat{C}_m$ , therefore, the transitional  $\sigma_r$  does not change with the capillary number.

The different modes of time-averaged deformation, namely sphere, prolate and oblate spheroids can be plotted onto a phase diagram with conductivity ratio and frequency as the coordinates. Figure 5 is plotted with the boundary integral simulation results conducted for a fixed capillary number ( $Ca \lesssim 0.1$ ) showing different regions marked out for the different modes of deformation. The different regions that are marked out by color shades in the phase diagram show different modes of time-averaged prolate and oblate deformations, respectively, whereas the white region mostly at the right half of the phase diagram represents the undeformed sphere region. The phase diagram is constructed assuming the shape to be a sphere if the degree of deformation is less than 1% of the initial spherical shape. The prolate shapes in the phase diagram are obtained when  $\sigma_r > 1$ , due to tensile normal electric stress at the poles. For  $\sigma_r < 1$ , oblate shapes are seen at intermediate frequencies, that is  $t_{cap}^{-1} < \omega < t_{MW}^{-1}$  due to compressive normal stresses



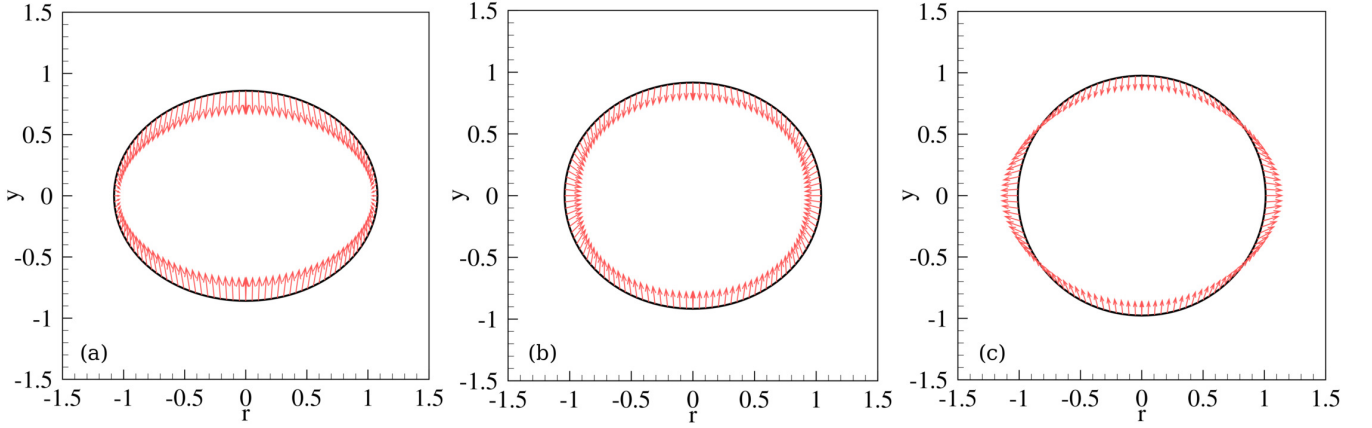


FIG. 6: In the limit of small capillary number ( $Ca = 0.1$ ) for  $\omega = 0.04$  and  $\sigma_r = 0.3$  (corresponding to the C-O breathing at high capillary number) considering  $\epsilon_r = 1$ ,  $G_m = 0$  and  $C_m = 50$ , electric stresses (arrows at the interface) are shown for the shapes observed during O-O breathing at  $t = 477, 496$  and  $515$ .

at the poles. At very high frequencies  $\omega > t_{MW}^{-1}$ , spherical shapes are seen for all the values of  $\sigma_r$ . For  $\sigma_r > 1$ , prolate shapes are seen for  $\omega < t_{cap}^{-1}$ , due to compressive normal electric stress at the equator.

Unlike the deformation of a capsule in DC fields which show time-independent deformation, the AC fields show time-dependent deformation which could be termed as "breathing" between two extreme shapes. Thus the phase diagram now exhibits different modes of breathing, namely prolate-prolate (P-P), prolate-sphere (P-S), prolate-oblate (P-O), oblate-sphere (O-S), oblate-oblate (O-O) and an undeformed sphere (S). The boundary integral simulation results (continuous curves) as well as, the results obtained from analytical theory (dashed curves) for a fixed capillary number ( $Ca = 0.1$ ) are shown in fig. 5. Numerically obtained phase boundaries separating zones for different breathing modes agree reasonably well with the analytically obtained results.

The temporal shape change of a capsule during an AC cycle is essentially because of the variation of the applied electric field with time. Thus, if the hydrodynamic and electric relaxation is fast as compared to the applied frequency, one can expect the behavior of a capsule in an AC field to be similar to the deformation of a capsule in a DC field of equivalent strength. In this limit, when the applied field goes to zero, the deformation too should go to zero, and only the prolate-sphere or oblate-sphere modes are expected. These modes of deformation are indeed seen in fig. 5 which also shows that the P-S and O-S modes of deformation are in agreement with the time-averaged regions of the phase diagram. However, when the hydrodynamic and electric relaxation timescales are of the same order or greater than the inverse of applied frequency, the instantaneous deformation need not be zero even when the instantaneous field is zero. This phenomena is, for example, illustrated by the P-P mode in the phase diagram (fig. 5). Interestingly the shape can

also change between two extremes, i.e., between prolate and oblate shapes and correspondingly, a variety of breathing modes can be obtained.

In general, the dynamics of a capsule in an AC field can be mapped on to the time evolution of a capsule in a DC field by realizing that the frequency in AC fields is identical to the inverse of time in DC fields. However, unique features typical of the AC fields can still be observed, which is due to the reversal of the electric field. Thus if the charge dynamics is slower than the applied frequency, a reversal of the sign of electric field (say, negative) can be observed, while the charge distribution continues to correspond to the earlier field (i.e., positive). This distributed charge causes a stress distribution over the interface and thereby, the deformation, which may not be seen in the corresponding DC fields.

Figures 6a-c show the stress distribution at the interface of a capsule at  $\sigma_r = 0.3$ . At the same conductivity ratio, fig. 7a represents the applied electric field and electric stress as a function of time and figs. 7b-h show the change of electrical variables on the interface of the capsule at different times. The compressive normal Maxwell stress at the poles leads to an oblate deformation. The normal electric stress at the poles is compressive on account of the higher conductivity of the external fluid medium. However, when the shape relaxes due to a decrease in the instantaneous field, the charge dynamics is such that although the applied electric field changes sign, the transmembrane potential does not. Figures 7b, e, f and h indicate that the  $\phi_m$  does not change sign even when the direction of the field is changed, e.g., negative  $\phi_m$  is seen at north pole even when the field is in the positive  $y$ -direction. This negative transmembrane potential leads to the tangential electric field inside being higher than that of the outside, leading to tensile normal electric stress. Such a phenomenon is not observed in DC field which does not switch direction. Although the

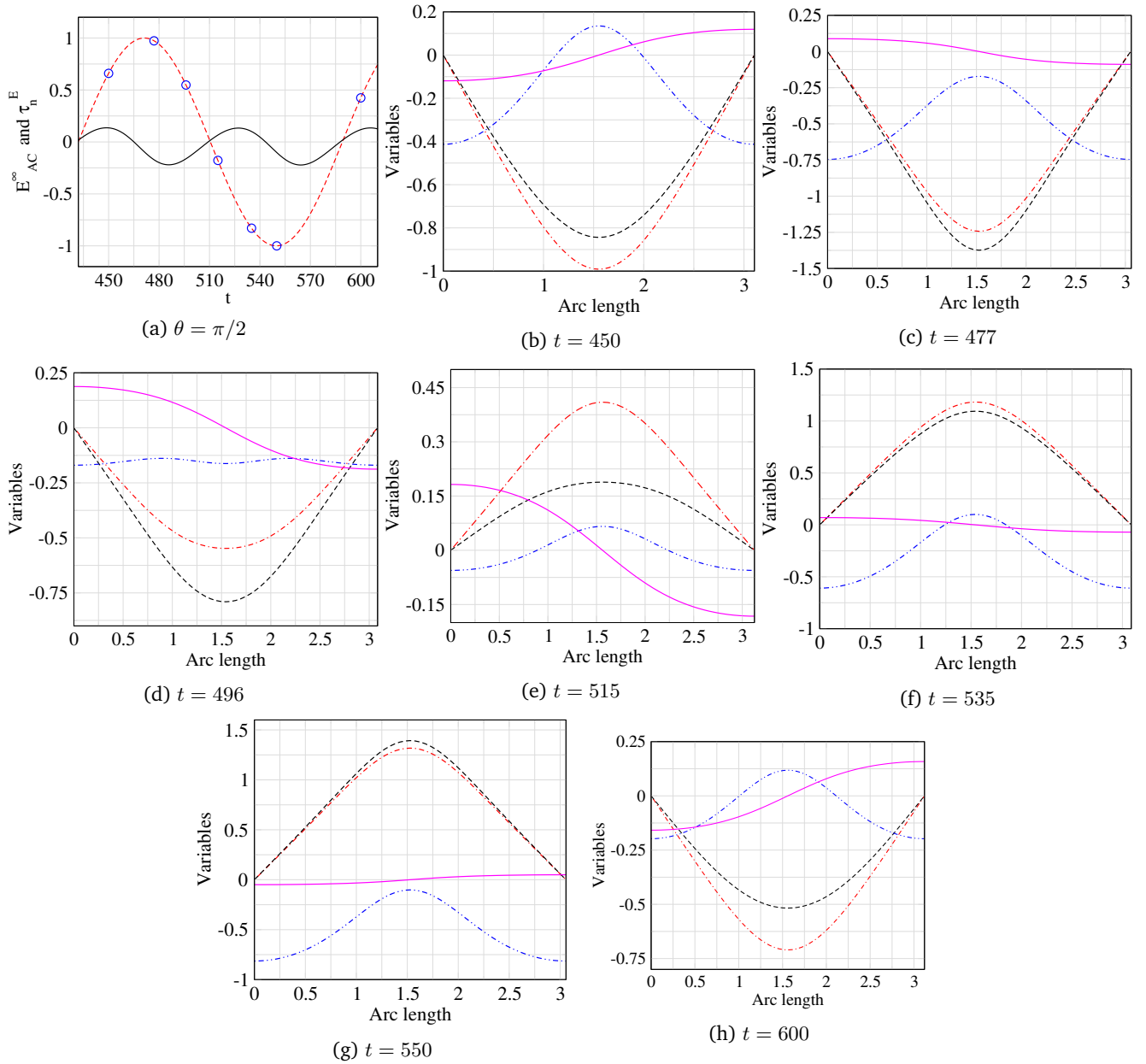


FIG. 7: In the limit of small deformation of a capsule ( $Ca = 0.1$ ) at  $\omega = 0.04$  and  $\sigma_r = 0.3$ , considering  $\epsilon_r = 1$ ,  $G_m = 0$  and  $C_m = 50$ , applied electric field (—) and the developed normal electric stress at the equator (—) as a function of time are shown in fig. (a), marker points show the instantaneous field for the subsequent figures. In other figures the variation of transmembrane potential (—), inner tangential electric field (---), outer tangential electric field (---) and normal electric stress (-.-.-) over the arc length are shown at the same conditions.

shape remains oblate leading to the O-O breathing mode (shown in fig. 18), the stress varies from compressive at the poles to tensile at the equator during a voltage cycle. Thus, the deformation modes in AC fields could have a very complex physical origin. The dynamics of the shapes in the P-O mode (shown in fig. 19) indicates that at low frequencies, the time-averaged oblate shape relaxes to a prolate shape within a voltage cycle. The stress distribution is seen to be a sensitive function of the

relative values of the membrane charging time and the Maxwell Wagner charge relaxation time with respect to the applied frequency (see figs. 6, figs. 20 and figs. 21).

A similar phase diagram (only the time-periodic) of a capsule deformation is observed at the high capillary number as shown in fig. 8. The small deformation and the large deformation phase boundaries in both the phase diagrams (fig. 5 and fig. 8) nearly overlap. The P-P, P-O, and O-O modes have a similar physical mech-



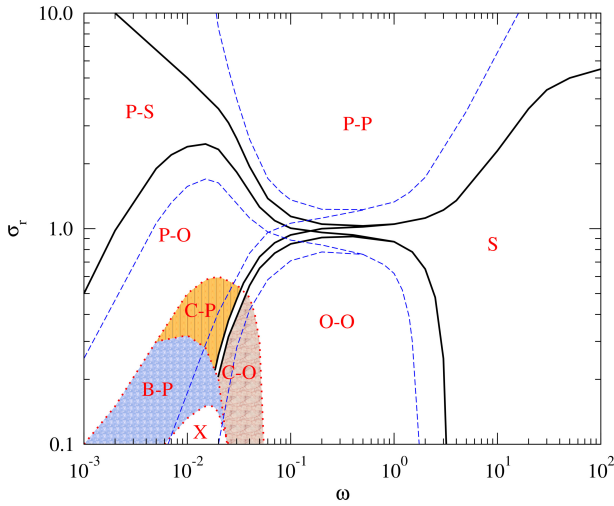


FIG. 8: Phase diagram of time-periodic breathing of capsule at  $Ca = 0.4$  considering  $\epsilon_r = 1$ ,  $G_m = 0$  and  $C_m = 50$  representing prolate-prolate breathing (P-P), prolate-sphere breathing (P-S), prolate-oblate breathing (P-O), oblate-oblate breathing (O-O) and undeformed sphere (S) zones of the deformation. Cylinder-prolate (C-P), cylinder-oblate (C-O), biconcave-prolate (B-P) and breakup (X) zones are shown with shades. Dashed curves are the boundaries separating zones of the phase diagram at  $Ca = 0.1$ .

anism as in the low capillary case. The large deformations encountered in these modes are shown in figures figs. 17 to 19 in the appendix. However, a significant deviation is observed in the range of  $10^{-3} \lesssim \omega \lesssim 0.5 \times 10^{-1}$  and  $0.1 \lesssim \sigma_r \lesssim 0.6$ . In this range of the frequency and conductivity ratio, new modes of complex breathing are observed, namely cylinder-prolate (C-P), cylinder-oblate (C-O), and biconcave-prolate (B-P).

Figures 9a-d show the shapes observed in cylindrical-prolate (C-P) breathing mode in a single time-period. The shapes shown correspond to the measured deformation at the marker points on the curve in fig. 9e and the corresponding instantaneous electric fields are shown by marker points on the curve in fig. 9f. Figures 10a-c show the hydrodynamic flow, variation of electric and elastic stresses at the interface, for the shapes in figs. 9a-c, respectively. The shape in fig. 9a is oblate since the outer medium is more conductive and  $t_{cap}^{-1} < \omega = 0.02 < t_{MW}^{-1}$ . A tensile azimuthal elastic tension at the equator (characteristic of an oblate shape) develops (inset of fig. 10a). The electric stresses are compressive at the poles (fig. 10a) assisting the formation of oblate shapes. The flow from the equator to the poles (in fig. 10a) shows a tendency of the capsule to return to a relaxed shape (fig. 9b). The high electric stress at the poles due to a highly nonlinear shape along with the compressive electric stress at the equator (fig. 10b) assist the formation of cylindrical shape (fig. 9b) while admitting an almost spherical shape (not shown here) at an intermedi-

ate time. The cylindrical shape is thus a manifestation of the high capillary number and corresponding interplay of high Maxwell stress and nonlinearity in shape (see figs. 10 and figs. 20). Towards the end of the cycle, the capsule assumes a prolate shape (fig. 9c) which is due to the developed Maxwell stress of a completely charged capacitor, the compressive normal electric stress with a maximum at the equator (fig. 10c). The elastic tensions are accordingly generated, with the azimuthal tension becoming negative at the equator (inset of fig. 10c). A tendency to attain oblate shape is then seen (fig. 9d) as the field reverses and the membrane discharges to attain an electrostatic solution commensurate with the applied field.

For a slightly lower conductivity and a higher frequency (as compared to fig. 9), observed shapes during the deformation are shown in figs. 11a-d. The corresponding degree of deformation and the instantaneous applied electric fields are shown by the marker points on curves in fig. 11e and f. A capsule attains cylinder-oblate spheroid (C-O) breathing mode at  $\sigma_r = 0.3$  and  $\omega = 0.04$ . Figures 12a-c show the state of electric stress, streamline, flow and elastic tensions (in insets) corresponding to figs. 11a-c, respectively. In this case, on account of relatively higher frequency (higher than the inverse of the membrane charging time) and lower conductivity ratio (compared to the C-P breathing), the capsule never relaxes to a sphere or a prolate shape. Only oblate shapes are admitted with flow from the equator to poles (figs. 12a and b) assisting the relaxation through the cylindrical shape (fig. 11b) to the oblate shape (fig. 11c). Pronounced tensile normal electric stresses are seen at the equator (fig. 12c) (a mechanism similar to that discussed in the low capillary limit, see figs. 6) that are responsible for the oblate shapes resulting in cylinder-oblate transition.

At much lower frequency though, a biconcave-prolate (B-P) breathing mode is observed (figs. 13a-d). The biconcave shape (fig. 13a) is the result of increased compressive Maxwell stress at the poles (fig. 14a), owing to higher conductivity contrast. Since the frequency is low, a relaxation to prolate shape is seen at the end of the cycle (fig. 13c) via an intermediate oblate shape (fig. 13b). This B-P breathing of capsule deformation is not observed at low capillary number as the electric stresses at the poles are insufficient (see figs. 21).

In this range of frequency ( $5 \times 10^{-3} \lesssim \omega \lesssim 2 \times 10^{-2}$ ) and at very low conductivity ratios, on account of greater charging of the membrane (the capsule acts more like a leaky dielectric drop), a highly compressive normal Maxwell stresses develop at the poles (e.g., fig. 15a). When the elastic tractions can not balance the developed electric stress at the pole, a capsule breaks up through the merging of poles. This breakup zone is marked with X in the phase diagram (fig. 8). Figure 15a confirms that within the valid range of numerical calculation, the developed elastic tensions at the pole just before breakup are very high (inset of fig. 15a). It should be

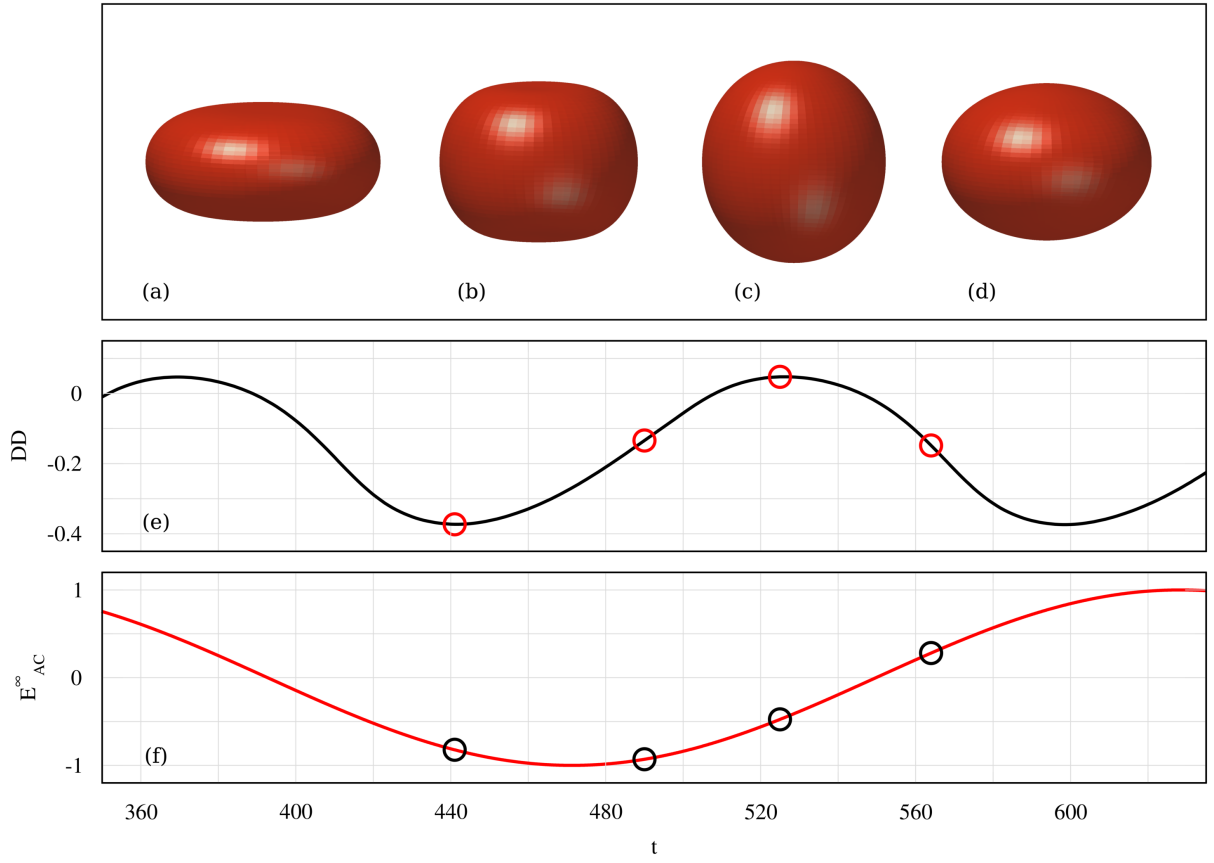


FIG. 9: Cylinder-prolate (C-P) breathing of a capsule (a-d) at  $Ca = 0.4$  for  $\omega = 0.02$  and  $\sigma_r = 0.4$  considering  $\epsilon_r = 1$ ,  $G_m = 0$  and  $C_m = 50$ . Shapes are corresponding to the marker points on the curves in (e) representing degree of deformation and in (f) representing applied electric field as the functions of time.

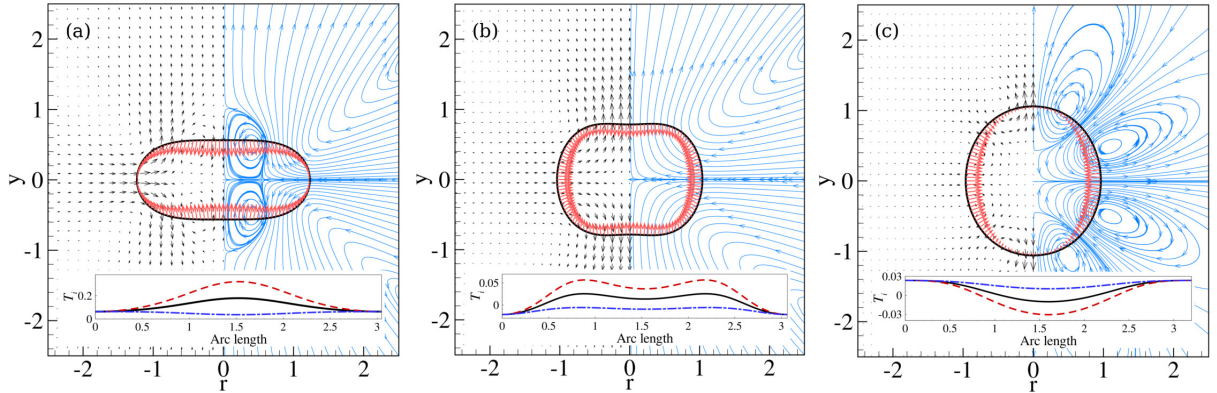


FIG. 10: Electric stress (shown by arrows at the interface), streamlines (shown only at right half) and velocity profile (shown only at left half, magnitude represents the relative extent of flow) for the shapes shown in fig. 9(a-c), respectively. The variation of meridional,  $T_s$  (— · —), azimuthal,  $T_\phi$  (— —) and mean,  $T_m$  (—) elastic tensions as a function of arc length are shown in insets.

noted that when the collocation points at poles come very close (closer than the element size used for the computation), the numerical computation is no more valid. Therefore, the shape observed in fig. 15b is actually a numerical artifact.

The modes of deformation of an elastic capsule with conducting membrane ( $\hat{G}_m = 10$ ) in AC electric field for  $Ca = 0.4$  is represented in fig. 16, keeping other param-

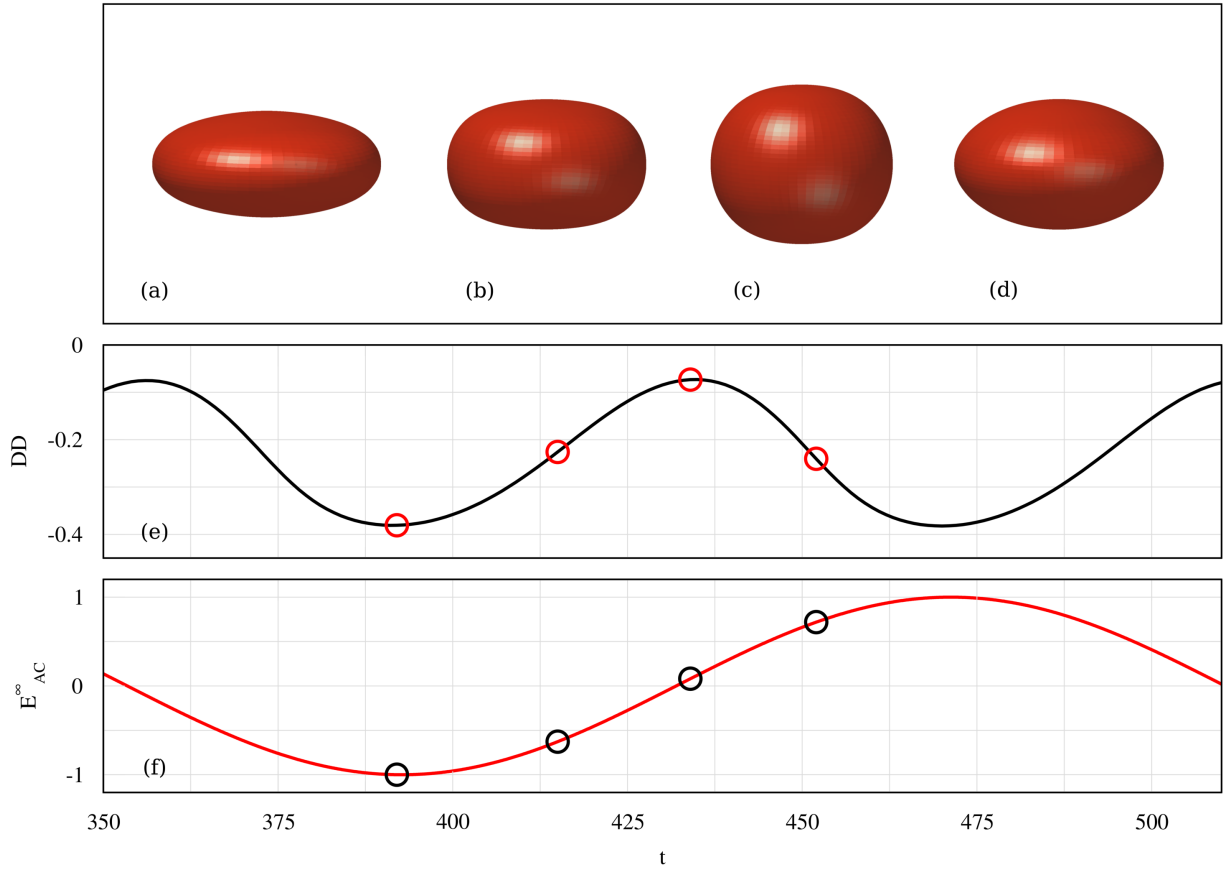


FIG. 11: Cylinder-oblate (C-O) breathing of a capsule (a-d) at  $Ca = 0.4$  for  $\omega = 0.04$  and  $\sigma_r = 0.3$  considering  $\epsilon_r = 1$ ,  $G_m = 0$  and  $C_m = 50$ . Shapes are corresponding to the marker points on the curves in (e) representing degree of deformation and in (f) representing applied electric field as the functions of time.

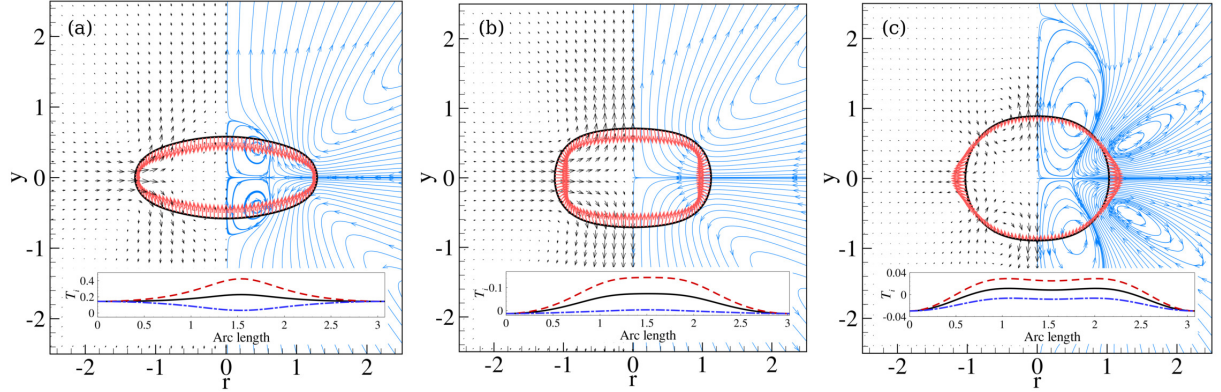


FIG. 12: Electric stress (shown by arrows at the interface), streamlines (shown only at right half) and velocity profile (shown only at left half, magnitude represents the relative extent of flow) for the shapes shown in fig. 11(a-c), respectively. The variation of meridional,  $T_s$  (— · —), azimuthal,  $T_\phi$  (— —) and mean,  $T_m$  (—) elastic tensions as a function of arc length are shown in insets.

eters unchanged, i.e.  $\epsilon_r = 1$  and  $\hat{C}_m = 50$ . In this case, a capsule does not exhibit any complex breathing mode in an AC field for the range of frequency  $10^{-3} \leq \omega \leq 10^2$  and conductivity ratio  $0.1 \leq \sigma_r \leq 10$ . The P-P, P-S, O-S

and O-O breathing modes are observed at low frequencies, but P-O breathing is not observed for this type of capsule. The high conductivity of the membrane in this case results in a capsule behaving like a leaky dielectric

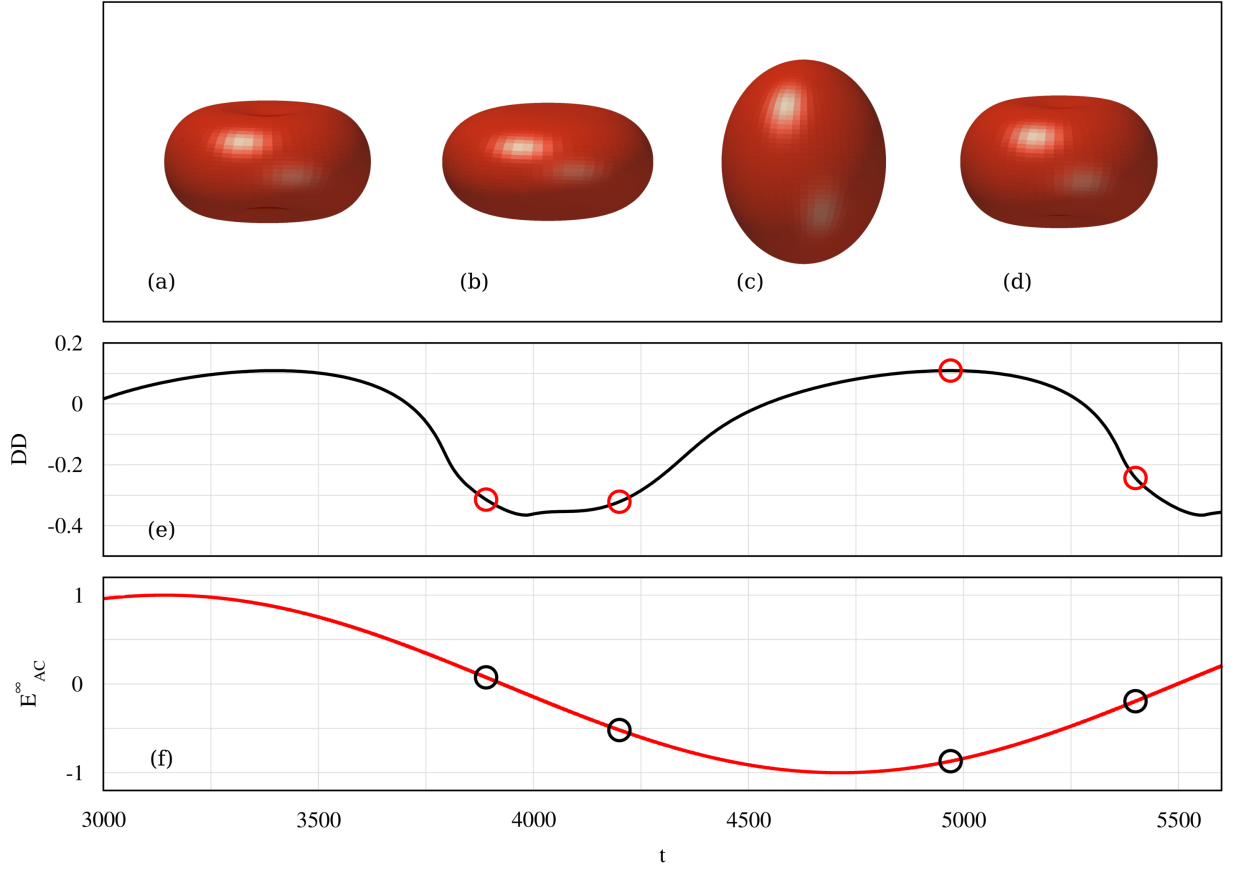


FIG. 13: Biconcave-prolate (B-P) breathing of a capsule (a-d) at  $Ca = 0.4$  for  $\omega = 0.002$  and  $\sigma_r = 0.1$  considering  $\epsilon_r = 1$ ,  $G_m = 0$  and  $C_m = 50$ . Shapes are corresponding to the marker points on the curves in (e) representing degree of deformation and in (f) representing applied electric field as the functions of time.

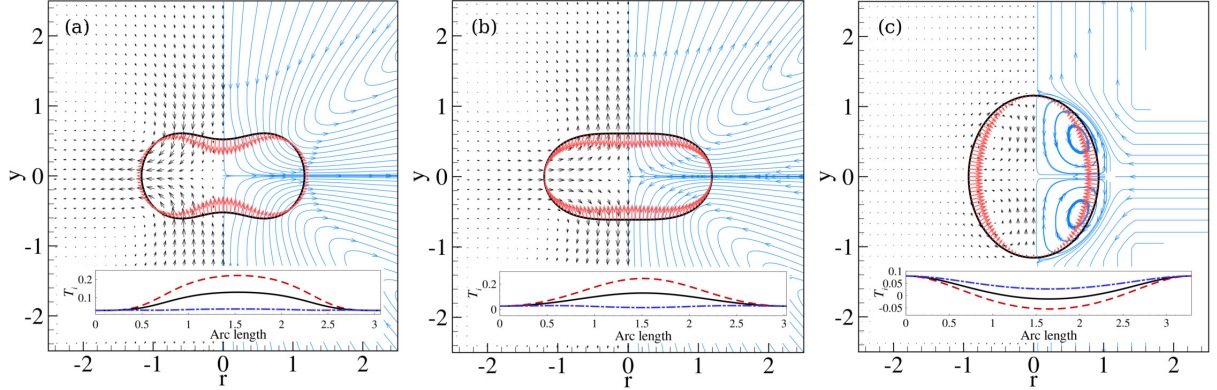


FIG. 14: Electric stress (shown by arrows at the interface), streamlines (shown only at right half) and velocity profile (shown only at left half, magnitude represents the relative extent of flow) for the shapes shown in fig. 13(a-c), respectively. The variation of meridional,  $T_s$  (— · —), azimuthal,  $T_\phi$  (---) and mean,  $T_m$  (—) elastic tensions as a function of arc length are shown in insets.

drop in a leaky dielectric medium. Thus, cylindrical or biconcave shapes are not observed since the stress remains highly compressive only at the poles, lacking any contribution from the equator.

## V. Conclusions

A phase diagram is constructed using boundary integral method and analytical theory at a low capillary number. It is found that the time-averaged deformation



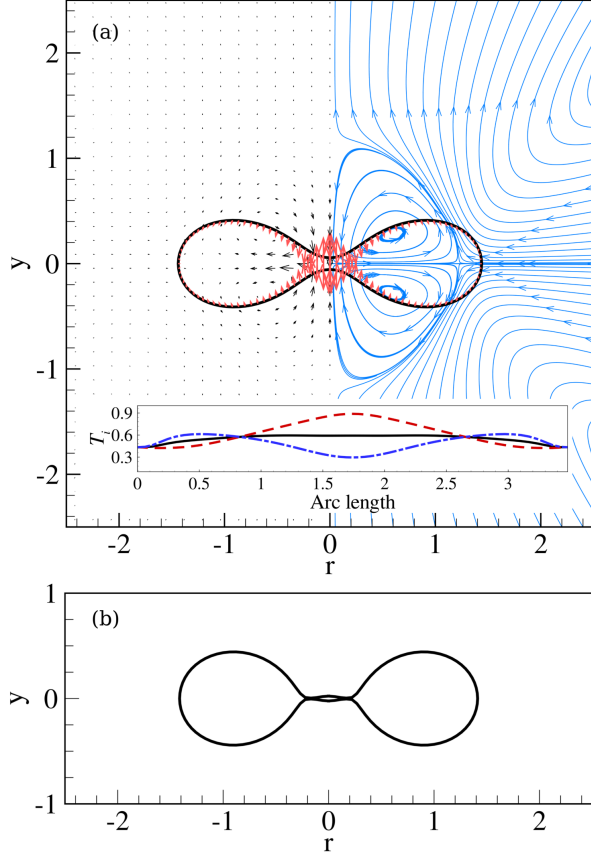


FIG. 15: Breakup of an elastic capsule at  $Ca = 0.4$  for  $\omega = 0.02$  and  $\sigma_r = 0.1$  considering  $\epsilon_r = 1$ ,  $G_m = 0$  and  $C_m = 50$ . (a) Electric stress (shown by arrows at the interface), streamlines (shown only at right half) and velocity profile (shown only at left half, magnitude represents the relative extent of flow) for the shape at the onset of break up (coordinates are assigned for the shape of the capsule). The variation of meridional,  $T_s$  ( $-\cdot-$ ), azimuthal,  $T_\phi$  ( $--$ ) and mean,  $T_m$  ( $—$ ) elastic tensions as a function of arc length are shown in insets. (b) Shape obtained from the numerical simulation just before the failure of the boundary integral code suggesting the breakup of the capsule through the merging of poles.

depends upon the frequency of the applied electric field and its value relative to the  $t_{MW}^{-1}$  and  $t_{cap}^{-1}$ . The time-periodic deformation shows breathing modes characterized as P-P, P-O, and O-O at a low capillary number. A high capillary number causes further bifurcation to highly nonlinear C-P, C-O, and B-P modes of deformation, attributed to strong coupling between charge density and electrostatics.

The proposed experiments to observe the theoretical results presented in this work could be on a thin Ovalbumin or human serum albumin (HSA) capsules of ra-

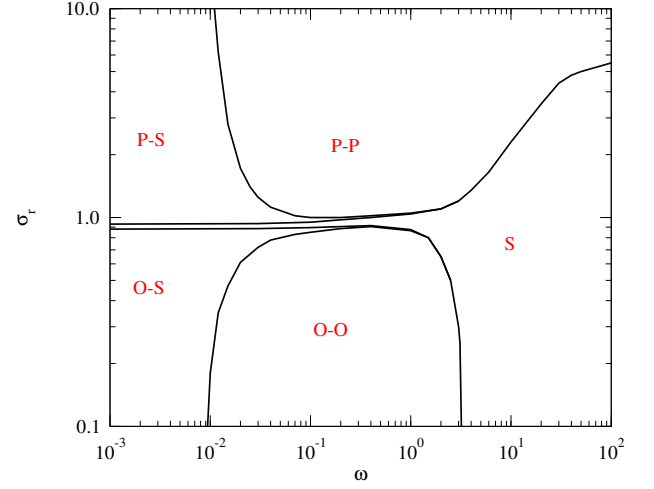


FIG. 16: Phase diagram of time-periodic breathing of capsule at  $Ca = 0.4$  considering  $\epsilon_r = 1$ ,  $G_m = 10$  and  $C_m = 50$  representing prolate-prolate breathing (P-P), prolate-sphere breathing (P-S), oblate-sphere breathing (O-S), oblate-oblate breathing (O-O) and undeformed sphere (S) zones of deformation.

dius  $a \simeq 500 \mu m$  with elasticity  $E_s \simeq 0.1 N/m$  [8], in an external fluid medium with conductivity  $\sigma_e \simeq 0.1 mS/m$ . In these experimental conditions, the typical field strength  $E_0 < 5 kV/cm$  and the frequencies in the range of  $[100 Hz - 10 MHz]$  should show the phenomenon described in this work.

This work is the simplest system that can demonstrate a strong shape-electrostatic-elastic-hydrodynamic coupling, which is important in electrohydrodynamics of soft matter. Findings of this work can form the basis for understanding large electro-elasto-hydrodynamics of more complicated soft matter systems, such as RBC, which will be the project for future communication.

#### Acknowledgment

Authors would like to thank the Department of Science and Technology (DST), Govt. of India, for financial support.

#### A. Analytical theory for electrohydrodynamic deformation of a capsule in the limit of small deformation

To seek an analytical solution in the small deformation limit, a spherical coordinate system is considered  $(r, \theta, \phi)$ , where  $r$  is the radial measurement from the center,  $\theta$  is the measurement of meridional angle and  $\phi$  is the measurement of azimuthal angle. In the axisymmetric analysis, assuming  $\theta = 0$  as the axis of symmetry, variations of quantities are independent of azimuthal angle.

The nondimensional potential due to the applied electric field in spherical coordinate system is expressed by

$$\phi^\infty = -\cos(\omega t)r \cos \theta \quad (A1)$$

which can be written as

$$\bar{\phi}^\infty = -\frac{1}{2}(e^{j\omega t} + e^{-j\omega t})r \cos \theta. \quad (\text{A2})$$

Henceforth, a variable  $\bar{x}$  is represented as a function of  $x$  and its conjugate  $x^*$  as

$$\bar{x} = \frac{1}{2}(xe^{j\omega t} + xe^{-j\omega t}). \quad (\text{A3})$$

Potential for the interior and exterior of the capsule satisfy the Laplace's equation,

$$\frac{1}{r^2} \frac{r^2 \frac{\partial \phi_{i,e}}{\partial r}}{\partial r} + \frac{1}{r^2 \sin \theta} \frac{\partial \left( \sin \theta \frac{\partial \phi_{i,e}}{\partial \theta} \right)}{\partial \theta} = 0 \quad (\text{A4})$$

where

$$\bar{\phi}_{i,e} = \frac{1}{2} [\phi_{i,e} e^{j\omega t} + \phi_{i,e}^* e^{-j\omega t}] \quad (\text{A5})$$

Internal and external potentials are expressed by spheri-

cal harmonics,

$$\phi_e = \phi^\infty + \frac{A_1}{r^2} P_1(\cos \theta) \quad (\text{A6})$$

$$\phi_i = A_2 r P_1(\cos \theta), \quad (\text{A7})$$

where,  $A_1$  and  $A_2$  are arbitrary constants, and  $P_1(\cos \theta)$  is the first order Legendre polynomial of  $\cos \theta$ . Transmembrane potential is defined as

$$\phi_m = \phi_{amp} \cos(\theta) = \phi_i - \phi_e \quad (\text{A8})$$

Current continuity in the normal direction is given by

$$\sigma_r E_{n,i} + \epsilon_r \frac{dE_{n,i}}{dt} = E_{n,e} + \frac{dE_{n,e}}{dt} = \hat{C}_m \frac{d\phi_m}{dt} + \hat{G}_m \phi_m \quad (\text{A9})$$

Coefficients  $A_1$ ,  $A_2$  and the transmembrane potential,  $\phi_m$ , can be obtained from the solutions of eq. (A6) and eq. (A7) using the definition of transmembrane potential (eq. (A8)) and the current continuity (eq. (A9)). The solution for the transmembrane potential of a spherical capsule with a nonconducting membrane is obtained as

$$\phi_m = 3 \cos \theta \frac{2(1 + \omega^2)(\omega^2 \epsilon_r^2 + \sigma_r^2) + \omega^2 [\epsilon_r \{2 + \omega^2(2 + \epsilon_r)\} + \sigma_r^2] \hat{C}_m}{4\sigma_r^2 + \omega^2 \{4(\epsilon_r^2 + \sigma_r^2) + 4(2\epsilon_r + \sigma_r^2) \hat{C}_m + (2 + \sigma_r)^2 \hat{C}_m^2\} + \omega^4 \{2\hat{C}_m + \epsilon_r(2 + \hat{C}_m)\}^2} \cos(\omega t) + \omega \{ \sigma_r(2 + \sigma_r) + \omega^2(\epsilon_r^2 + 2\sigma_r) \} \hat{C}_m \sin(\omega t), \quad (\text{A10})$$

with a phase lag

$$\alpha = -\arctan \left[ \frac{\omega(\sigma_r(2 + \sigma_r) + \omega^2(\epsilon_r^2 + 2\sigma_r)) \hat{C}_m}{2(1 + \omega^2)(\omega^2 \epsilon_r^2 + \sigma_r^2) + \omega^2 [\epsilon_r \{2 + \omega^2(2 + \epsilon_r)\} + \sigma_r^2] \hat{C}_m} \right] \quad (\text{A11})$$

Electric fields in  $r$  and  $\theta$  directions at the interface are determined as

$$E_{r,i} = -\frac{\partial \phi_i}{\partial r} \quad (\text{A12a})$$

$$E_{\theta,i} = -\frac{1}{r} \frac{\partial \phi_i}{\partial \theta} \quad (\text{A12b})$$

$$E_{r,e} = -\frac{\partial \phi_e}{\partial r} \quad (\text{A12c})$$

$$E_{\theta,e} = -\frac{1}{r} \frac{\partial \phi_e}{\partial \theta}. \quad (\text{A12d})$$

The Maxwell electric stress tensor is given by  $\hat{\mathbf{T}}^E = \epsilon(\hat{\mathbf{E}}\hat{\mathbf{E}} - \frac{1}{2}\hat{E}^2\mathbf{I})$ , where  $\hat{E}^2$  is the inner product of the field, and  $\mathbf{I}$  is the identity tensor. The normal and tangential components of the electric traction can be obtained by

$$\tilde{f}_r = \mathbf{n} \cdot \hat{\mathbf{T}}^E \cdot \mathbf{n} = \frac{1}{2} \epsilon \epsilon_0 (\tilde{E}_r^2 - \tilde{E}_\theta^2) \quad (\text{A13a})$$

$$\tilde{f}_\theta = \mathbf{t} \cdot \hat{\mathbf{T}}^E \cdot \mathbf{n} = \epsilon \epsilon_0 \tilde{E}_r \tilde{E}_\theta \quad (\text{A13b})$$

such that  $\tilde{\mathbf{f}}^E = \tilde{f}_r \mathbf{e}_r + \tilde{f}_\theta \mathbf{e}_\theta$  is the total electric traction acting at the interface. For an undeformed sphere, normal vector  $\mathbf{n} = \mathbf{e}_r$  and the tangent vector  $\mathbf{t} = \mathbf{e}_\theta$ . Using eqs. A12 with the eq. (A5), dimensionless tractions can be expressed as

$$\begin{aligned} \bar{f}_r = \frac{1}{8} [ & 2E_{re}E_{re}^* - 2E_{\theta e}E_{\theta e}^* + (E_{re}^2 - E_{\theta e}^2)e^{2j\omega t} + (E_{re}^* - E_{\theta e}^*)e^{-2j\omega t} ] \\ & - \frac{\epsilon_r}{8} [ 2E_{ri}E_{ri}^* - 2E_{\theta i}E_{\theta i}^* + (E_{ri}^2 - E_{\theta i}^2)e^{2j\omega t} + (E_{ri}^* - E_{\theta i}^*)e^{-2j\omega t} ] \end{aligned} \quad (\text{A14a})$$

$$\begin{aligned} \bar{f}_\theta = \frac{1}{4} [ & (E_{re}E_{\theta e}^* + E_{re}^*E_{\theta e}) + (E_{re}E_{\theta e}e^{2j\omega t} + E_{re}^*E_{\theta e}^*e^{-2j\omega t}) ] \\ & - \frac{\epsilon_r}{4} [ (E_{ri}E_{\theta i}^* + E_{ri}^*E_{\theta i}) + (E_{ri}E_{\theta i}e^{2j\omega t} + E_{ri}^*E_{\theta i}^*e^{-2j\omega t}) ]. \end{aligned} \quad (\text{A14b})$$



Tractions can also be expressed as

$$f_r = f_{rs} + \frac{1}{2} [f_{rt}e^{2j\omega t} + f_{rt}^*e^{-2j\omega t}] \quad (\text{A15a})$$

$$f_\theta = f_{\theta s} + \frac{1}{2} [f_{\theta t}e^{2j\omega t} + f_{\theta t}^*e^{-2j\omega t}], \quad (\text{A15b})$$

where subscripts  $s$  and  $t$  represent time-averaged and time-periodic parts. Time-averaged electric tractions are obtained as

$$f_{rs} = \frac{1}{4} [E_{re}E_{re}^* - E_{\theta e}E_{\theta e}^*] - \frac{\epsilon_r}{4} [E_{ri}E_{ri}^* - E_{\theta i}E_{\theta i}^*], \quad (\text{A16a})$$

$$f_{\theta s} = \frac{1}{4} [E_{re}E_{\theta e}^* + E_{re}^*E_{\theta e}] - \frac{\epsilon_r}{4} [E_{ri}E_{\theta i}^* + E_{ri}^*E_{\theta i}] \quad (\text{A16b})$$

and time-periodic electric tractions are

$$f_{rt} = \frac{1}{4} [(E_{re}^2 - E_{\theta e}^2) - \epsilon_r(E_{ri}^2 - E_{\theta i}^2)], \quad (\text{A17a})$$

$$f_{\theta t} = \frac{1}{2} [E_{re}E_{\theta e} - \epsilon_r E_{ri}E_{\theta i}], \quad (\text{A17b})$$

where  $f_{rs}$ ,  $f_{\theta s}$  are real and  $f_{rt}$ ,  $f_{\theta t}$  are complex quanti-

ties.

Calculation of elastic traction, hydrodynamics formulation, and solution procedure are followed as reported in our earlier article [51]. In general, the expressions for the degree of deformation as a function of frequency and capillary number are very complex. For a nonconducting ( $G_m = 0$ ) membrane, the time-averaged degree of deformation is obtained as

$$DD_s = \frac{9}{32} Ca \frac{(5(\epsilon_r^2 + \sigma_r^2) + 2\hat{C}_m(5\epsilon_r + 3\sigma_r^2) + \hat{C}_m^2\{5 - 16\epsilon_r + \sigma_r(6 + 5\sigma_r)\})\omega^2}{4\sigma_r^2 + (4(\hat{C}_m + \epsilon_r)^2 + 4\hat{C}_m^2\sigma_r + (2 + \hat{C}_m)^2\sigma_r^2)\omega^2 + (2\epsilon_r + \hat{C}_m(2 + \epsilon_r))^2\omega^4}, \quad (\text{A18})$$

and the time-periodic degree of deformation for a special

case considering  $G_m = 0$ ,  $C_m = 50$ ,  $\epsilon_r = 1$  is obtained as

$$DD_t = \frac{45Ca}{32} \left[ \sigma_r^2 + 6\sigma_r(17 + 11\sigma_r)j\omega + \{5399 - \sigma_r(3732 + 2869\sigma_r)\}\omega^2 - 2\{\sigma_r(12319 + 5152\sigma_r) - 16167\}j\omega^3 \right. \\ \left. + (36008\sigma_r - 33731)\omega^4 + 704j\omega^5 \right] / \left[ \{35\omega(10\omega - 3j) - 4\}\{(51 + 76j\omega)\omega + \sigma_r(26\omega - j)\}^2 \right]. \quad (\text{A19})$$

The deformation of an elastic capsule, in the limit of

small deformation, can be obtained from

$$DD = DD_s + \left[ \frac{DD_t e^{2j\omega t} + DD_t^* e^{-2j\omega t}}{2} \right], \quad (\text{A20})$$

where  $DD_t^*$  is the complex conjugate of  $DD_t$ .

[1] D. Barthès-Biesel. Motion of a spherical microcapsule freely suspended in a linear shear flow. *Journal of Fluid*

*Mechanics*, 100(4):831–853, 10 1980.  
[2] D. Barthès-Biesel. Role of interfacial properties on the

- motion and deformation of capsules in shear flow. *Physica A: Statistical Mechanics and its Applications*, 172(1):103 – 124, 1991.
- [3] D. Barthès-Biesel and V. Chhim. The constitutive equation of a dilute suspension of spherical microcapsules. *International Journal of Multiphase Flow*, 7(5):493 – 505, 1981. ISSN 0301-9322.
- [4] D. Barthès-Biesel and J. M. Rallison. The time-dependent deformation of a capsule freely suspended in a linear shear flow. *Journal of Fluid Mechanics*, 113:251–267, 12 1981.
- [5] Dominique Barthès-Biesel, Anna Diaz, and Emmanuelle Dhenin. Effect of constitutive laws for two-dimensional membranes on flow-induced capsule deformation. *Journal of Fluid Mechanics*, 460:211–222, 2002.
- [6] H Brøndsted, C Andersen, and L Hovgaard. Crosslinked dextran - a new capsule material for colon targeting of drugs. *Journal of Controlled Release*, 53(1-3):7 – 13, 1998.
- [7] K. S. Chang and W. L. Olbricht. Experimental studies of the deformation of a synthetic capsule in extensional flow. *Journal of Fluid Mechanics*, 250:587–608, 005 1993.
- [8] T.X. Chu, A.-V. Salsac, E. Leclerc, D. Barthès-Biesel, H. Wurtz, and F. Edwards-Lévy. Comparison between measurements of elasticity and free amino group content of ovalbumin microcapsule membranes: Discrimination of the cross-linking degree. *Journal of Colloid and Interface Science*, 355(1):81 – 88, 2011. ISSN 0021-9797.
- [9] Joseph M. Crowley. Electrical breakdown of bimolecular lipid membranes as an electromechanical instability. *Biophysical Journal*, 13(7):711 – 724, 1973.
- [10] Sudip Das and Rochish Thaokar. Large deformation electrohydrodynamics of an elastic capsule in dc electric field. *ArXiv e-prints*, Aug. 2017. <https://arxiv.org/abs/1708.08802>.
- [11] C. de Loubens, J. Deschamps, G. Boedec, and M. Leonetti. Stretching of capsules in an elongation flow, a route to constitutive law. *Journal of Fluid Mechanics*, 767, 2015.
- [12] Katherine A. DeBruin and Wanda Krassowska. Modeling electroporation in a single cell. i. effects of field strength and rest potential. *Biophysical Journal*, 77(3):1213 – 1224, 1999.
- [13] A. Diaz, N. Pelekasis, and D. Barthès-Biesel. Transient response of a capsule subjected to varying flow conditions: Effect of internal fluid viscosity and membrane elasticity. *Physics of Fluids*, 12(5):948–957, 2000.
- [14] Rumiana Dimova, Karin A. Riske, Said Aranda, Natalya Bezlyepkina, Roland L. Knorr, and Reinhard Lipowsky. Giant vesicles in electric fields. *Soft Matter*, 3:817–827, 2007.
- [15] W. R. Dodson and P. Dimitrakopoulos. Dynamics of strain-hardening and strain-softening capsules in strong planar extensional flows via an interfacial spectral boundary element algorithm for elastic membranes. *Journal of Fluid Mechanics*, 641:263–296, 2009.
- [16] R. Finken, S. Kessler, and U. Seifert. Micro-capsules in shear flow. *Journal of Physics: Condensed Matter*, 23(18): 184113, 2011.
- [17] Constantino Grosse and Herman P. Schwan. Cellular membrane potentials induced by alternating fields. *Biophysical Journal*, 63(6):1632 – 1642, 1992.
- [18] Jong-Wook Ha and Seung-Man Yang. Electrohydrodynamic effects on the deformation and orientation of a liquid capsule in a linear flow. *Physics of Fluids*, 12(7): 1671–1684, 2000.
- [19] W. Helfrich. Elastic properties of lipid bilayers: Theory and possible experiments. *Z Naturforschung C*, 28:693, 1973.
- [20] W. Helfrich. Lipid bilayer spheres: Deformation and birefringence in magnetic fields. *Physics Letters A*, 43(5):409 – 410, 1973.
- [21] W. Helfrich. Deformation of lipid bilayer spheres by electric fields. *Z Naturforschung C*, 29:182, 1974.
- [22] W.-F. Hu, M.-C. Lai, Y. Seol, and Y.-N. Young. Vesicle electrohydrodynamic simulations by coupling immersed boundary and immersed interface method. *Journal of Computational Physics*, 317:66 – 81, 2016.
- [23] Wei-Fan Hu, Yongsam Kim, and Ming-Chih Lai. An immersed boundary method for simulating the dynamics of three-dimensional axisymmetric vesicles in navier-stokes flows. *Journal of Computational Physics*, 257, Part A:670 – 686, 2014.
- [24] Rahul B. Karyappa, Shivraj. D. Deshmukh, and Rochish. M. Thaokar. Deformation of an elastic capsule in a uniform electric field. *Physics of Fluids*, 26(12):122108, 2014.
- [25] S. Kessler, R. Finken, and U. Seifert. Elastic capsules in shear flow: Analytical solutions for constant and time-dependent shear rates. *The European Physical Journal E*, 29(4):399–413, Aug 2009. ISSN 1292-895X.
- [26] Ebrahim M. Kolahdouz and David Salac. Electrohydrodynamics of three-dimensional vesicles: A numerical approach. *SIAM Journal on Scientific Computing*, 37(3): B473–B494, 2015.
- [27] Ebrahim M. Kolahdouz and David Salac. Dynamics of three-dimensional vesicles in dc electric fields. *Phys. Rev. E*, 92:012302, Jul 2015.
- [28] M. Kummrow and W. Helfrich. Deformation of giant lipid vesicles by electric fields. *Phys. Rev. A*, 44:8356–8360, Dec 1991.
- [29] Sehoon Kwak and C. Pozrikidis. Effect of membrane bending stiffness on the axisymmetric deformation of capsules in uniaxial extensional flow. *Physics of Fluids*, 13(5): 1234–1242, 2001.
- [30] E. Lac, D. Barthès-Biesel, N. A. Pelekasis, and J. Tsamopoulos. Spherical capsules in three-dimensional unbounded stokes flows: effect of the membrane constitutive law and onset of buckling. *Journal of Fluid Mechanics*, 516:303–334, 10 2004.
- [31] Dennis Lensen, Dennis M. Vriezema, and Jan C. M. van Hest. Polymeric microcapsules for synthetic applications. *Macromolecular Bioscience*, 8(11):991–1005, 2008.
- [32] Stephen Mann, John P. Hannington, and R. J. P. Williams. Phospholipid vesicles as a model system for biomineralization. *Nature*, 324:565–567, 12 1986.
- [33] P. Marszalek, D.S. Liu, and T.Y. Tsong. Schwan equation and transmembrane potential induced by alternating electric field. *Biophysical Journal*, 58(4):1053 – 1058, 1990.
- [34] Lane C. McConnell, Michael J. Miksis, and Petia M. Vlahovska. Vesicle electrohydrodynamics in dc electric fields. *IMA Journal of Applied Mathematics*, 78(4):797, 2013.
- [35] Lane C. McConnell, Michael J. Miksis, and Petia M. Vlahovska. Continuum modeling of the electric-field-induced tension in deforming lipid vesicles. *The Journal of Chemical Physics*, 143(24):243132, 2015.
- [36] Lane C. McConnell, Petia M. Vlahovska, and Michael J. Miksis. Vesicle dynamics in uniform electric fields: squaring and breathing. *Soft Matter*, 11:4840–4846, 2015.

- [37] A.E. Neumann, E. Sowers and C.A. Jordan. *Electroporation and Electrofusion in Cell Biology*. Plenum press, New York, 1 edition, 1989.
- [38] Primoz Peterlin. Frequency-dependent electrodeformation of giant phospholipid vesicles in ac electric field. *Journal of Biological Physics*, 36(4):339–354, Sep 2010.
- [39] Ronald Pethig. Dielectrophoresis: Using inhomogeneous ac electrical fields to separate and manipulate cells. *Critical Reviews in Biotechnology*, 16(4):331–348, 1996.
- [40] C. Pozrikidis. *Boundary integral and singularity methods for linearized viscous flow*. Cambridge university press, New York, 1992.
- [41] C. Pozrikidis. Finite deformation of liquid capsules enclosed by elastic membranes in simple shear flow. *Journal of Fluid Mechanics*, 297:123–152, 008 1995.
- [42] J. M. Rallison and A. Acrivos. A numerical study of the deformation and burst of a viscous drop in an extensional flow. *Journal of Fluid Mechanics*, 89:191–200, 11 1978.
- [43] Karin A. Riske and Rumiana Dimova. Electric pulses induce cylindrical deformations on giant vesicles in salt solutions. *Biophysical Journal*, 91(5):1778 – 1786, 2006.
- [44] Thomas Schnelle, Rolf Hagedorn, Günter Fuhr, Stefan Fiedler, and Torsten Müller. Three-dimensional electric field traps for manipulation of cells - calculation and experimental verification. *Biochimica et Biophysica Acta (BBA) - General Subjects*, 1157(3):127 – 140, 1993.
- [45] H. P. Schwan. *Biophysics of the Interaction of Electromagnetic Energy with Cells and Membranes*, pages 213–231. Springer US, Boston, MA, 1983. ISBN 978-1-4684-4253-3.
- [46] Udo Seifert. Configurations of fluid membranes and vesicles. *Advances in Physics*, 46(1):13–137, 1997.
- [47] Jacopo Seiwert and Petia M. Vlahovska. Instability of a fluctuating membrane driven by an ac electric field. *Phys. Rev. E*, 87:022713, Feb 2013.
- [48] Jacopo Seiwert, Michael J. Miksis, and Petia M. Vlahovska. Stability of biomimetic membranes in dc electric fields. *Journal of Fluid Mechanics*, 706:58–70, 2012.
- [49] R. Skalak, A. Tozeren, R.P. Zarda, and S. Chien. Strain energy function of red blood cell membranes. *Biophysical Journal*, 13(3):245 – 264, 1973.
- [50] Pascal Tanner, Patric Baumann, Ramona Enea, Ozana Onaca, Cornelia Palivan, and Wolfgang Meier. Polymeric vesicles: From drug carriers to nanoreactors and artificial organelles. *Accounts of Chemical Research*, 44(10):1039–1049, 2011. PMID: 21608994.
- [51] Rochish M. Thaokar. Time-dependent electrohydrodynamics of a compressible viscoelastic capsule in the small-deformation limit. *Phys. Rev. E*, 94:042607, Oct 2016.
- [52] D. Peter Tieleman. The molecular basis of electroporation. *BMC Biochemistry*, 5(1):10, Jul 2004.
- [53] L. N. Trefethen. *Finite difference and spectral methods for ordinary and partial differential equations*. Unpublished text: <http://web.comlab.ox.ac.uk/oucl/work/nick.trefethen/pdtext.html>, 1996.
- [54] Shravan Veerapaneni. Integral equation methods for vesicle electrohydrodynamics in three dimensions. *Journal of Computational Physics*, 326:278 – 289, 2016.
- [55] P. M. Vlahovska, Y.-N. Young, G. Danker, and C. Misbah. Dynamics of a non-spherical microcapsule with incompressible interface in shear flow. *Journal of Fluid Mechanics*, 678:221–247, 2011.
- [56] Petia M. Vlahovska, Rubèn Serral Gracià, Said Aranda-Espinoza, and Rumiana Dimova. Electrohydrodynamic model of vesicle deformation in alternating electric fields. *Biophysical Journal*, 96(12):4789 – 4803, 2009.
- [57] S. Wallace, D. Yang, M. Wallace, C. Li, and L.R. Kuang. Therapeutic and diagnostic use of modified polymeric microcapsules, January 16 1996. US Patent 5,484,584.
- [58] M Winterhalter and W Helfrich. Deformation of spherical vesicles by electric fields. *Journal of Colloid and Interface Science*, 122(2):583 – 586, 1988.
- [59] Ranhua Xiong, Stefaan J. Soenen, Kevin Braeckmans, and Andre G. Skirtach. Towards theranostic multicompartment microcapsules: in-situ diagnostics and laser-induced treatment. *Theranostics*, 3:141–151, 2013.
- [60] Xiaoming Yang, Tingyang Dai, Min Wei, and Yun Lu. Polymerization of pyrrole on a polyelectrolyte hollow-capsule microreactor. *Polymer*, 47(13):4596 – 4602, 2006. ISSN 0032-3861.
- [61] Ou-Yang Zhong-can and Wolfgang Helfrich. Bending energy of vesicle membranes: General expressions for the first, second, and third variation of the shape energy and applications to spheres and cylinders. *Phys. Rev. A*, 39: 5280–5288, May 1989.

### B. Supplementary information

The prolate-prolate breathing (P-P) of an elastic capsule at  $\omega = 0.1$  and  $\sigma_r = 5$ , is shown in figs. 17a and b. The degrees of deformation of the shapes shown in figs. 17a and b are shown with the marker points on the curve in fig. 17c and the corresponding instantaneous applied electric field is shown in fig. 17d. This example of P-P breathing is corresponding to the zone presented in the high capillary number phase diagram in fig. 8.

Similar to the case of P-P breathing, a capsule with the  $\sigma_r$  in the O-O zone, experience oblate-oblate breathing in AC electric field. As an example, the shapes at the minima and maxima of the electric stress in the O-O breathing at  $Ca = 0.4$  for  $\omega = 0.4$  and  $\sigma_r = 0.1$  are shown in figs. 18a and b. The degree of deformation of these shapes are shown by the marker points on the deformation curve (fig. 18b) and the corresponding instantaneous electric fields are shown by the marker points on the curve in fig. 18c.

At very low frequency and conductivity ratio of O-O zone, (for an example, at  $Ca = 0.4$  for  $\omega = 0.01$  and 0.8) the extreme shapes in P-O breathing are shown in figs. 19a and b which are corresponding to the deformations, shown by the marker point on the curve in fig. 19c and the corresponding instantaneous electric fields are shown by marker points on the curve in (fig. 19)d.

At a small capillary number ( $Ca = 0.1$ ) the distribution of electric stress at the interface for  $\omega = 0.02$  and  $\sigma_r = 0.4$  is shown in fig. 20 undergoing O-S breathing and the same is shown for  $\omega = 0.002$  and  $\sigma_r = 0.1$  in fig. 21 representing P-O breathing of a capsule. Figures 20 and 21 are shown at the combinations of  $\omega$  and  $\sigma_r$  which are corresponding to the C-P and B-P breathing modes, respectively, at a high capillary number.

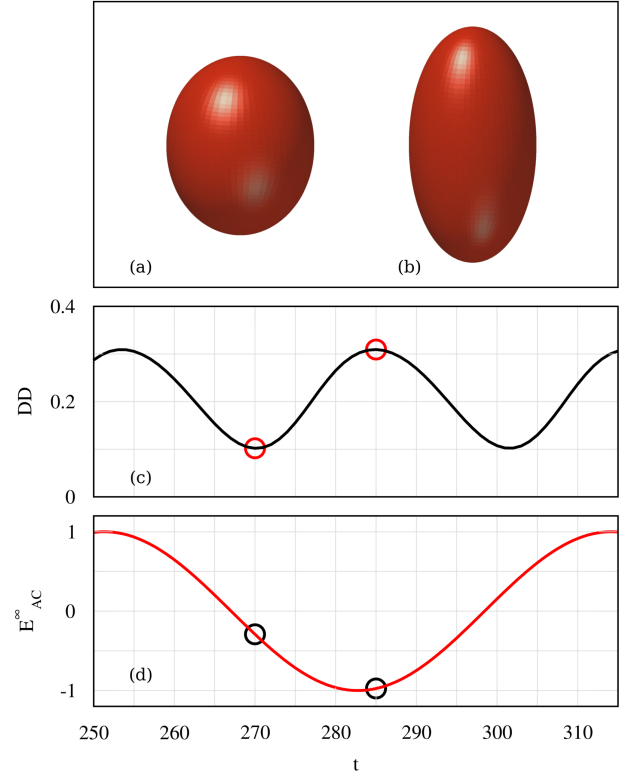


FIG. 17: P-P breathing of a capsule at  $Ca = 0.4$  for  $\omega = 0.1$  and  $\sigma_r = 5$ , considering  $\epsilon_r = 1$ ,  $G_m = 0$  and  $C_m = 50$ . Shapes are corresponding to the marker points on the curves in (c) representing the degree of deformation and in (d) representing applied electric field as the functions of time.

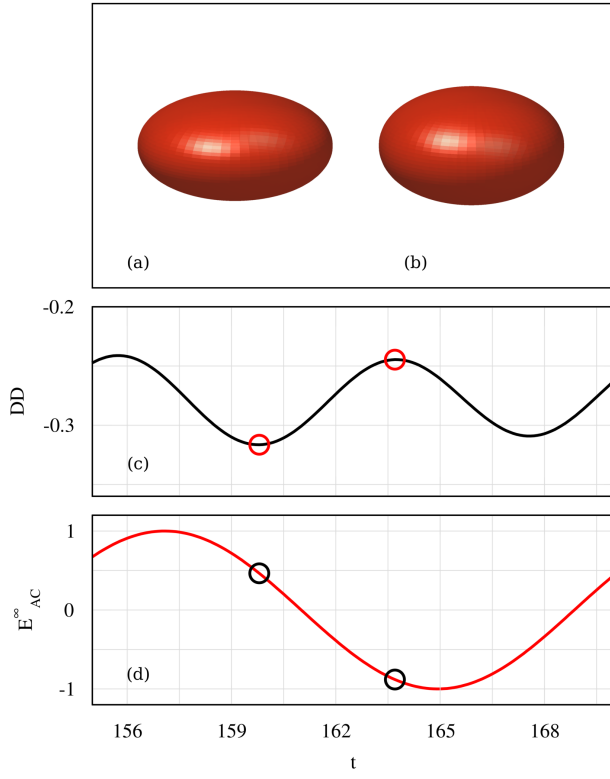


FIG. 18: O-O breathing of a capsule at  $Ca = 0.4$  for  $\omega = 0.4$  and  $\sigma_r = 0.1$ , considering  $\epsilon_r = 1$ ,  $G_m = 0$  and  $C_m = 50$ . Shapes are corresponding to the marker points on the curves in (c) representing the degree of deformation and in (d) representing applied electric field as the functions of time.

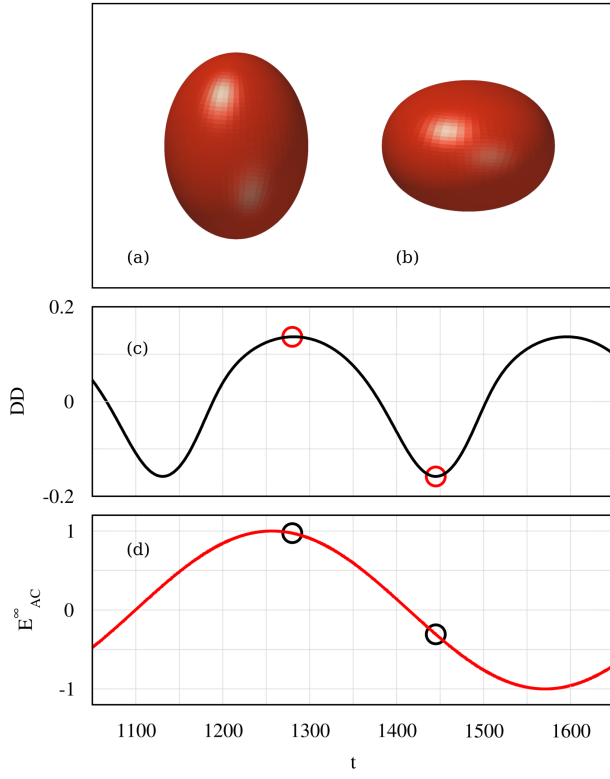


FIG. 19: P-O breathing of a capsule at  $Ca = 0.4$  for  $\omega = 0.01$  and  $\sigma_r = 0.8$ , considering  $\epsilon_r = 1$ ,  $G_m = 0$  and  $C_m = 50$ . Shapes are corresponding to the marker points on the curves in (c) representing the degree of deformation and in (d) representing applied electric field as the functions of time.

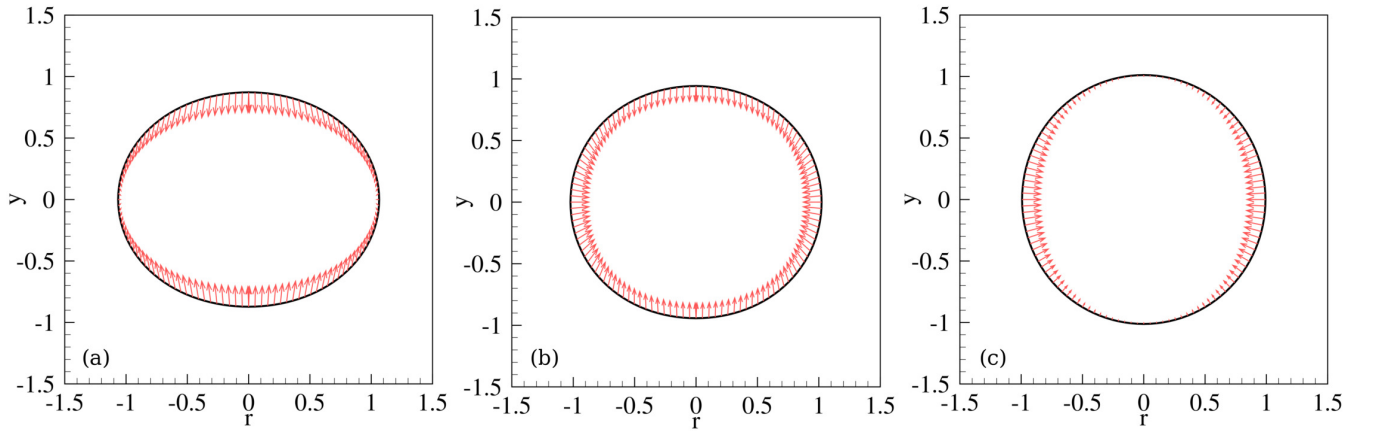


FIG. 20: In the limit of small capillary number ( $Ca = 0.1$ ) for  $\omega = 0.02$  and  $\sigma_r = 0.4$  (corresponding to the C-P breathing at high capillary number) considering  $\epsilon_r = 1$ ,  $G_m = 0$  and  $C_m = 50$ , the electric stresses (arrows at the interface) are shown for the shapes observed during O-S breathing.



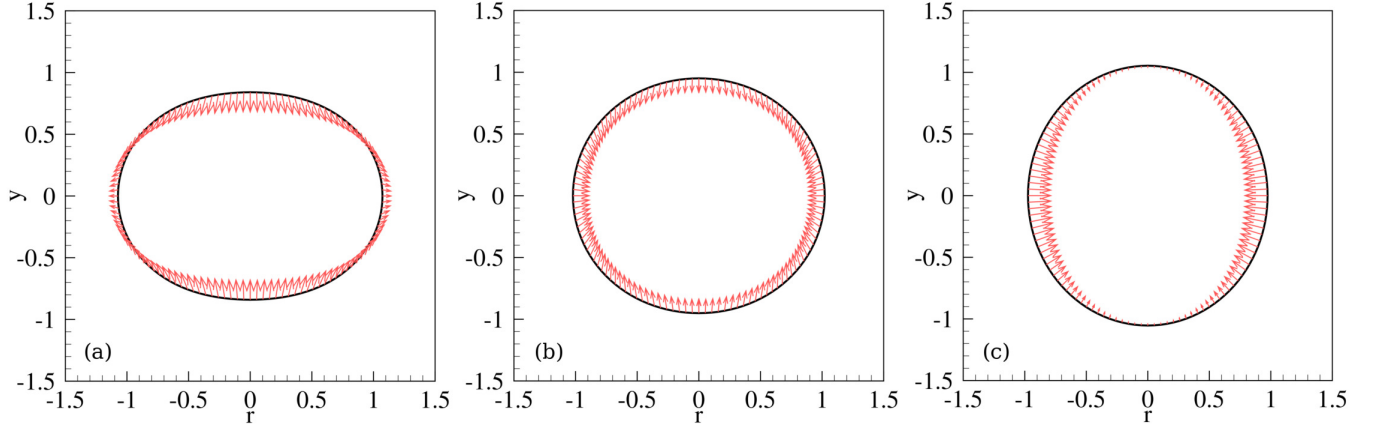


FIG. 21: In the limit of small capillary number ( $Ca = 0.1$ ) for  $\omega = 0.002$  and  $\sigma_r = 0.1$  (corresponding to the B-P breathing at high capillary number) considering  $\epsilon_r = 1$ ,  $G_m = 0$  and  $C_m = 50$ , the electric stresses (arrows at the interface) are shown for the shapes observed during P-O breathing.